



OPEN

# PTEN deficiency in postnatally developing Purkinje cells disrupts metabolic signaling, leading to dendritic abnormalities and sex-specific behavioral deficits

Lindsay J. Walsh, Izabella M. Espinal-San Miguel, Ana V. Rodriguez, Ursula M. Peña, Kiley E. Flynn, Will C. Remillard, Siena R. Brazier, Natalia I. Anderson, Aidan J. Clark, Tiffany A. De Varona & Ileana Soto<sup>✉</sup>

Conditional deletion of the *Pten* gene in cerebellar Purkinje cells (PCs) results in cellular hypertrophy, neurodegeneration, and autism-like behaviors in adult mice. Here, we investigated the effects of PTEN conditional deficiency on PC dendritic development and early postnatal motor, spontaneous, and social behaviors. We found that *Pten* loss disrupts dendritic growth by altering mTOR signaling and reducing AMPK phosphorylation, leading to early motor deficits and sex-specific behavioral alterations. *In vivo* analysis revealed significant reductions in mitochondrial and lysosomal volume in developing dendrites. Notably, *ex vivo* treatment with AICAR (an AMPK activator) or Torin1 (an mTOR inhibitor) partially restored dendritic organelle content in *Pten*-deficient PCs. These findings suggest that PTEN is critical for maintaining metabolic balance during postnatal dendritic maturation, and its loss leads to structural and functional impairments in PCs that contribute to behavioral phenotypes in a sex- and age-dependent manner.

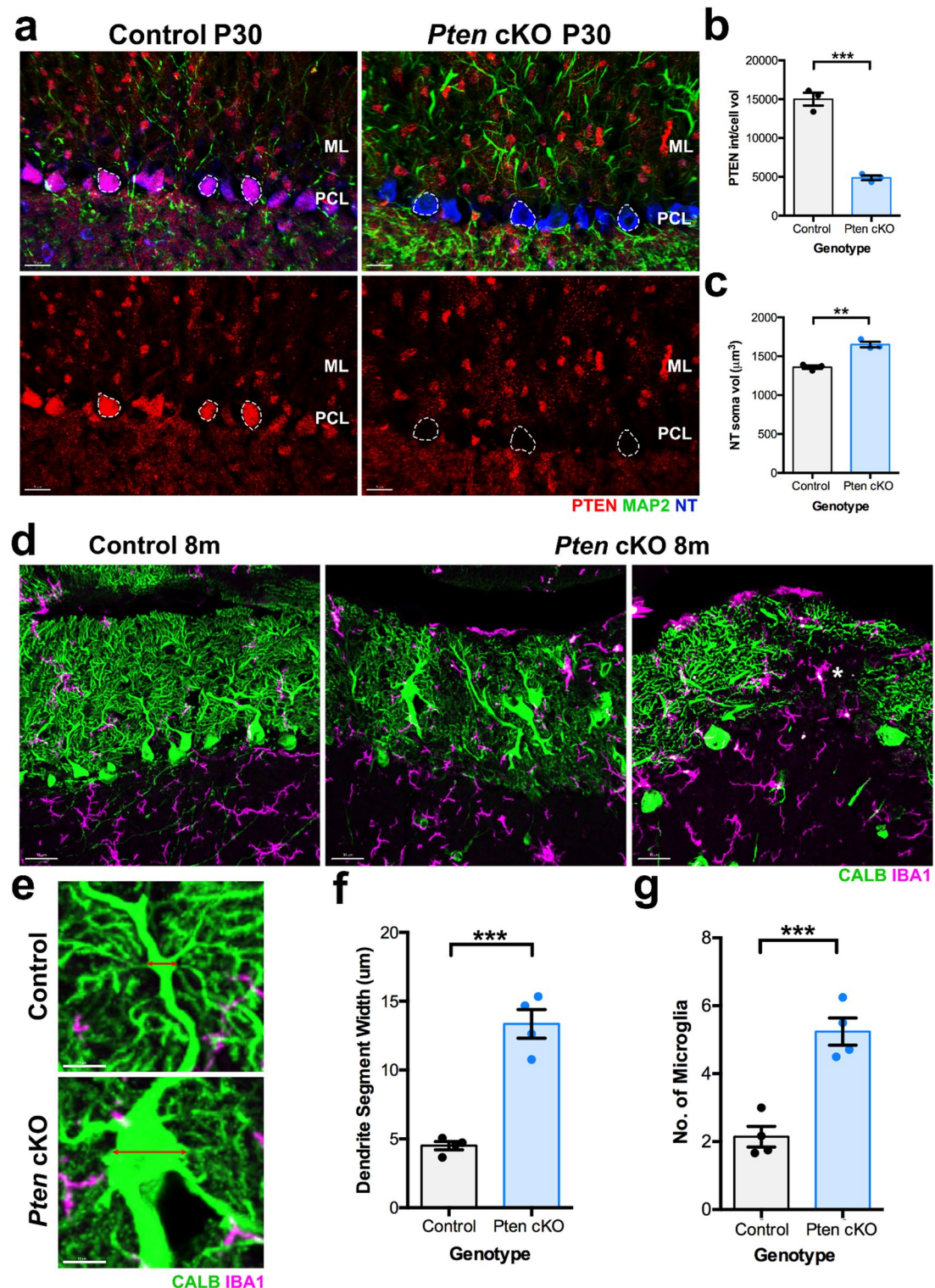
**Keywords** PTEN, Purkinje cells, mTORC1, Mitochondria, Lysosomes, AMPK, AICAR, Torin1

Approximately 25–50% of children with PTEN mutations are diagnosed with autism spectrum disorder (ASD)<sup>1,2</sup>. PTEN-ASD is characterized by reduced PTEN protein levels, lower IQ, impaired adaptive and motor functions, and social attention deficits<sup>3</sup>. In mice, PTEN haploinsufficiency or neuron-specific deletion leads to macrocephaly, neuronal hypertrophy, and ASD-like behaviors<sup>4–11</sup>. Conditional deletion of *Pten* in cerebellar PCs results in soma and dendritic hypertrophy, mTORC1 hyperactivation, and autistic-like traits in adult males<sup>12</sup> highlighting the cerebellum's role in PTEN-ASD. Given the cerebellum's involvement in motor, cognitive, and social functions, its dysfunction is strongly implicated in ASD pathophysiology<sup>13–15</sup>. Deletion of other ASD-related genes in PCs also induces autism-like behaviors<sup>16–20</sup> further supporting their relevance. Additionally, the *Pten* cKO PC model recapitulates ASD-associated cerebellar abnormalities, including structural changes, reduced PC size with age, PC loss, and altered social behaviors<sup>21</sup>.

Since lack of *Pten* in PCs leads to significant changes in dendrites and behavioral traits associated with ASD in adult male mice, we inquired about the impact of the lack of this gene in the postnatal development of PC dendrites and early mouse behaviors. Given that the extension and patterning of high-volume dendrites with large surface areas are energy-intensive processes requiring the synthesis of complex biomolecules<sup>22,23</sup> localized metabolic regulation is presumed to play a critical role in dendritic development. An important regulator of metabolic pathways is the mTORC1, an evolutionarily conserved nutrient sensor that is the center of signaling networks that regulate cellular metabolic processes and growth<sup>24</sup>. Growing evidence has implicated the TORC1 pathway in the dendritic growth of mouse hippocampal<sup>11,25</sup>, cortical<sup>11,26</sup> and Purkinje<sup>20,27</sup> neurons, suggesting a primary role of metabolic regulation in dendritic differentiation.

PTEN is an endogenous inhibitor of the PI3 kinase, which produces PIP3 (phosphatidylinositol (3,4,5) and activates AKT<sup>28,29</sup>. As a serine/threonine kinase, AKT activates the mTORC1 pathway and plays a critical role in cell growth, survival, and metabolism<sup>29</sup>. Developmental changes in PTEN-deficient neurons suggest a critical role of PTEN in the regulation of the AKT/mTORC1 pathway during neuronal development<sup>25–27</sup>. Previous

Department of Biology, Providence College, Providence, RI, USA. <sup>✉</sup>email: isotorey@providence.edu



work in our laboratory demonstrated that conditional haploinsufficiency of *Pten* (*Pten* cHet) in PCs leads to the overactivation of the AKT-mTORC1 pathway and the overgrowth of dendrites at postnatal day 14<sup>30</sup>. However, by P30, the dendritic tree of *Pten* cHet PCs is slightly smaller than control PCs, supporting the regulatory role of the PTEN-AKT-mTORC1 pathway in dendritic development. In this study, we examined the effects of complete *Pten* deletion on postnatal PC dendritic development. PTEN-deficient PCs displayed significant disruptions in dendritic growth and structure, including neurofilament accumulation and reduced synaptic density. These structural abnormalities were associated with impaired motor skill acquisition across early and late postnatal stages, as well as changes in social and non-social behaviors. Mechanistically, PTEN loss dysregulated mTORC1 and AMPK signaling, leading to mitochondrial and lysosomal deficits in dendrites. Notably, ex vivo treatment with an AMPK activator or mTOR inhibitor restored mitochondrial content, underscoring the metabolic role of PTEN in PC dendritic maturation.

**Fig. 1.** PTEN deficiency in PCs leads to dendritic degeneration and increased microglia in the ML. **(a)** PTEN immunofluorescence (red) in the soma (NT-blue) of PCs and other cells in the ML from P30 Control and *Pten* cKO mice. MAP2 immunofluorescence (green) in PC dendrites. **(b)** Quantitative analysis of PTEN immunofluorescence intensity per NT cell volume in PCs from P30 Control and *Pten* cKO mice. **(c)** Quantitative analysis of NT PC soma volume from P30 Control and *Pten* cKO mice. **(d)** Degeneration and hypertrophy of CALB<sup>+</sup> PC soma and dendrites accompanied by increased activation of IBA1<sup>+</sup> microglia in 8 m *Pten* cKO mice. **(e)** Magnified view of a CALB<sup>+</sup> PC dendrite in 8 m Control and *Pten* cKO mice, red line shows width difference between genotypes. **(f)** Quantitative analysis of dendrite segment width in 8 m Control and *Pten* cKO mice. **(g)** Quantitative analysis of the number of microglia in the ML of 8 m Control and *Pten* cKO mice. Data are presented as mean $\pm$ SEM,  $n=4$  mice/genotype, **(b,c)** 7–8 cells/mouse, **(f)** 5–6 images/mouse, **(g)** 48 segments/genotype. \*\* $P<0.01$  and \*\*\* $P<0.001$ , by unpaired *t*-test. Scale bar: **(a)** 20  $\mu$ m, **(d)** 30  $\mu$ m, **(e)** 10  $\mu$ m. *ML* molecular layer, *PCL* Purkinje cell layer.

## Results

### PTEN deficiency alters Purkinje cell postnatal dendritic development

Postnatal brain development is marked by extensive dendritic growth and synaptogenesis<sup>31</sup>. Notably, PTEN protein levels are elevated in neonatal mouse brains compared to embryonic and adult stages<sup>32,33</sup> suggesting a critical role for this phosphatase in regulating neuronal development during the postnatal period. In control mice, PTEN immunoreactivity in PC somas was highest at postnatal day 14 (P14) and gradually declined by P21 and P30 (Fig. S1), suggesting a critical role for PTEN during periods of active dendritic growth and synaptogenesis in postnatal PCs. To investigate PTEN's role in postnatal PC development, we used a conditional knockout (cKO) mouse model in which PTEN was selectively deleted using the PCP2-Cre driver. This Cre driver becomes active during the first postnatal week, with approximately 80% recombination in PCs by P10 and near-complete recombination (100%) by P14<sup>34</sup>. To confirm that PCs in *Pten* cKO mice were the only cells in the cerebellum deficient of PTEN, immunofluorescence experiments were performed using antibodies against PTEN and MAP2 (to label dendrites) and fluorescent NeuroTrace (to label PC somas). Lack of PTEN immunoreactivity in PCs and increased PC soma volume were found in *Pten* cKO mice at P30 compared to control mice (Fig. 1a–c). Still, in *Pten* cKO mice, PTEN immunoreactivity was evident in other cells in the molecular layer (ML), confirming the conditional deletion of the *Pten* gene only in PCs (Fig. 1a). Additionally, when assessing aged adult (8 m) *Pten* cKO mice and as previously reported<sup>12</sup> we found large focal dendritic swellings that were three to six times wider than primary dendrites' width in adult (8 m) control mice (Fig. 1d–f). Also, along to the remarkable loss of CALB<sup>+</sup> PC dendrites at this stage (white asterisk, Fig. 1d), a significant increase in the number of IBA1<sup>+</sup> microglia in the ML of 8 m *Pten* cKO cerebella was also found (Fig. 1d and g), demonstrating the significant long-term impact of PTEN deficiency in PC dendrites.

Since PC dendrites are severely affected in adult *Pten* cKO mice, we interrogated the impact of PTEN deficiency in PC dendritic postnatal development, a highly metabolic dependent process. Using the Golgi-Cox staining, the growth and arborization of PC dendrites were assessed at postnatal ages 10, 14, and 30 days. At P10, Sholl quantitative analysis revealed a significant increase in the number of dendritic intersections at different distances from the soma in *Pten* cKO PCs when compared to control mice (Fig. 2a–c). The dendritic total length was also significantly higher in *Pten* cKO PCs than in control PCs at P10 (Fig. 2d). Unexpectedly, the number of dendritic intersections and total length were significantly reduced at P14 in *Pten* cKO PCs, and no differences between *Pten* cKO and control PCs were found at P30 (Fig. 2a–d). These results suggest that PTEN deficiency triggers an early postnatal burst in dendritic growth and arborization in PCs, which is not maintained into the second postnatal week. However, a partial recovery in dendritic growth appears during the third and fourth postnatal weeks, suggesting that the effects of PTEN deficiency on PC development are modulated by dynamic extrinsic factors, such as activity-dependent mechanisms, and intrinsic genetic programs that unfold across distinct developmental stages.

Although no significant differences were observed in the number of dendritic intersections or total dendritic length between *Pten* cKO and control mice at P30, additional pathological features were evident in the PC dendrites of *Pten* cKO mice. Quantitative analysis revealed a significant reduction in spine density (spines/ $\mu$ m) in P30 *Pten* cKO PCs compared to controls (Fig. 3a–b). Additionally, dendritic thickness was increased, as indicated by a larger fraction of the area occupied by dendrites within a defined region (Fig. 3a, c). Immunofluorescence analysis showed markedly increased neurofilament immunoreactivity in the dendrites of *Pten* cKO PCs at both P14 and P30 relative to controls (Fig. 3d–e), likely contributing to the observed dendritic thickening. Furthermore, the total volume of VGLUT2 + puncta, marking climbing fiber presynaptic terminals in the molecular layer, was significantly reduced in P30 *Pten* cKO mice (Fig. 3d, f), consistent with the observed loss of dendritic spines. Together, these findings suggest that early accumulation of cytoskeletal proteins such as neurofilaments contributes to dendritic dystrophy and synaptic deficits in *Pten* cKO PCs.

### PTEN deficiency in Purkinje cells alters postnatal motor function and behavior in mice

Since PTEN deficiency alters PC dendritic and synaptic postnatal development, we examined motor control at early and late postnatal stages. Mouse pups develop crawling behavior during the first week of age, whereas transition to walking occurs between 5 and 10 days of age<sup>35</sup>. Given the role of the cerebellum in motor balance and coordination, we sought to determine how *Pten* deficiency in PCs affects ambulation in P8 mouse pups. Using the ambulation test, a score system was applied to identify no movement, crawling, and transition as described previously<sup>35</sup>. In crawling, the whole back paw touches the ground when ambulating (Fig. 4a), while during transition there is some elevation at the heel of the back paw, but the head and tail are still low to the ground as

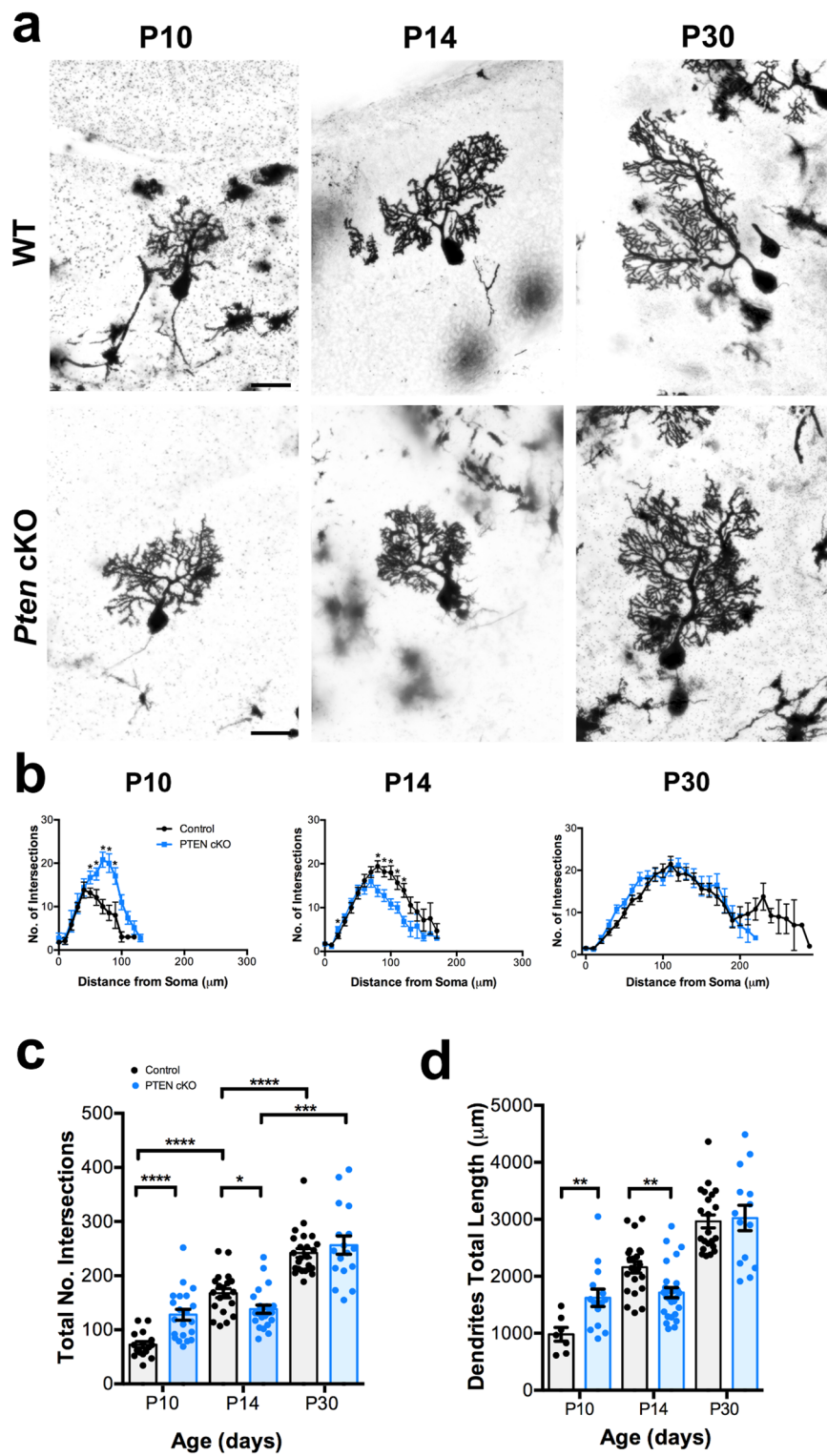


**Fig. 2.** *Pten* conditional deletion in PCs alters the postnatal development of their dendrites. **(a)** Golgi-Cox staining of PCs from Control and *Pten* cKO mice at P10, P14, and P30. **(b)** Sholl-analysis showing differences in PC dendritic branching between Control and *Pten* cKO mice at P10, P14, and P30. **(c)** Quantification of dendritic total intersections calculated by Sholl analysis in P10, P14, and P30 Control and *Pten* cKO mice. **(d)** Quantification of PC dendritic total length at P10, P14, and P30 in Control and *Pten* cKO mice. Data presented as mean  $\pm$  SEM,  $n=5$ –6 cells/mouse from 4–5 mice/genotype.  $^*P<0.05$ ,  $^{**}P<0.001$ ,  $^{***}P<0.001$ ,  $^{****}P<0.0001$ , by unpaired *t*-test. Scale bar: **(a)** 20  $\mu$ m.

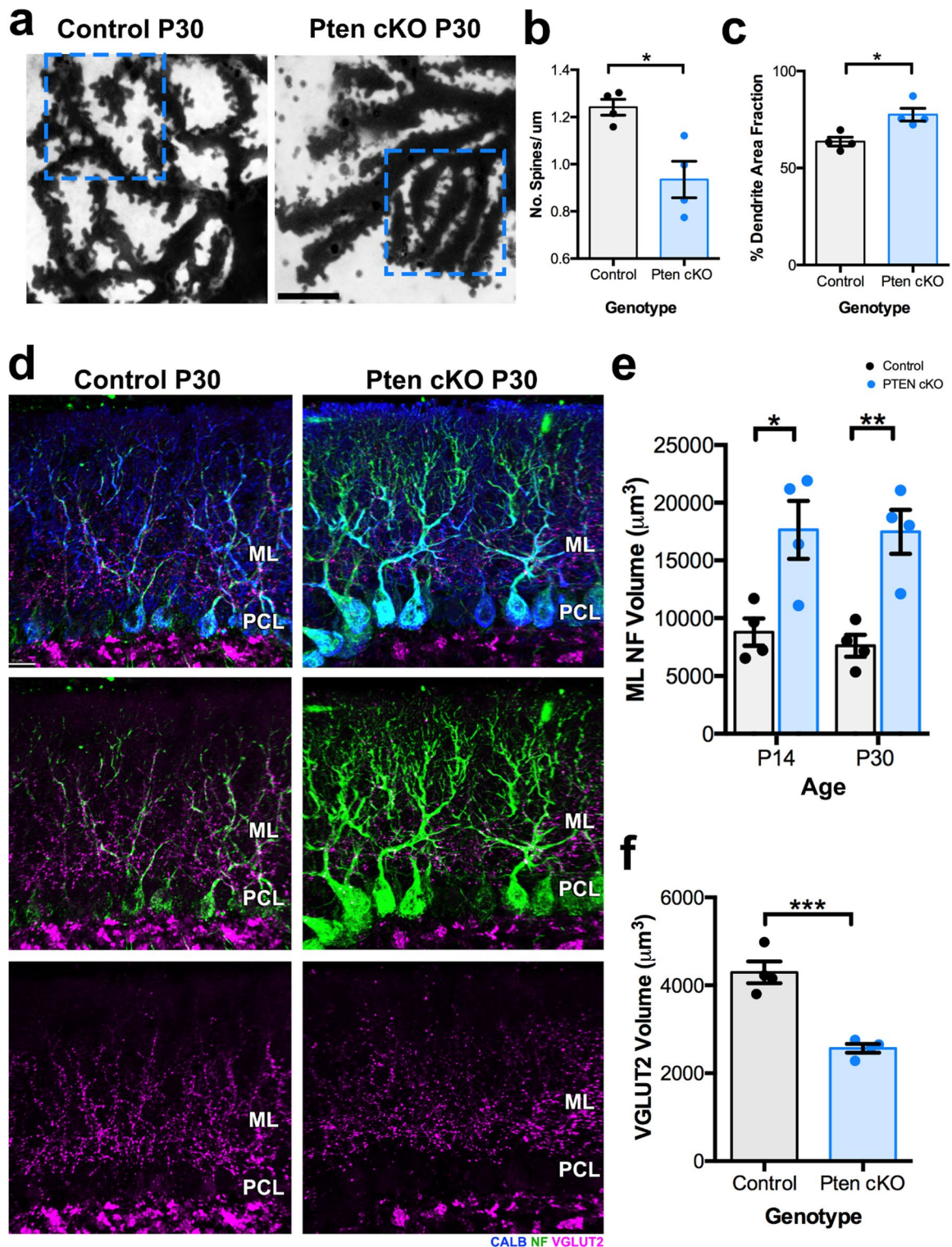
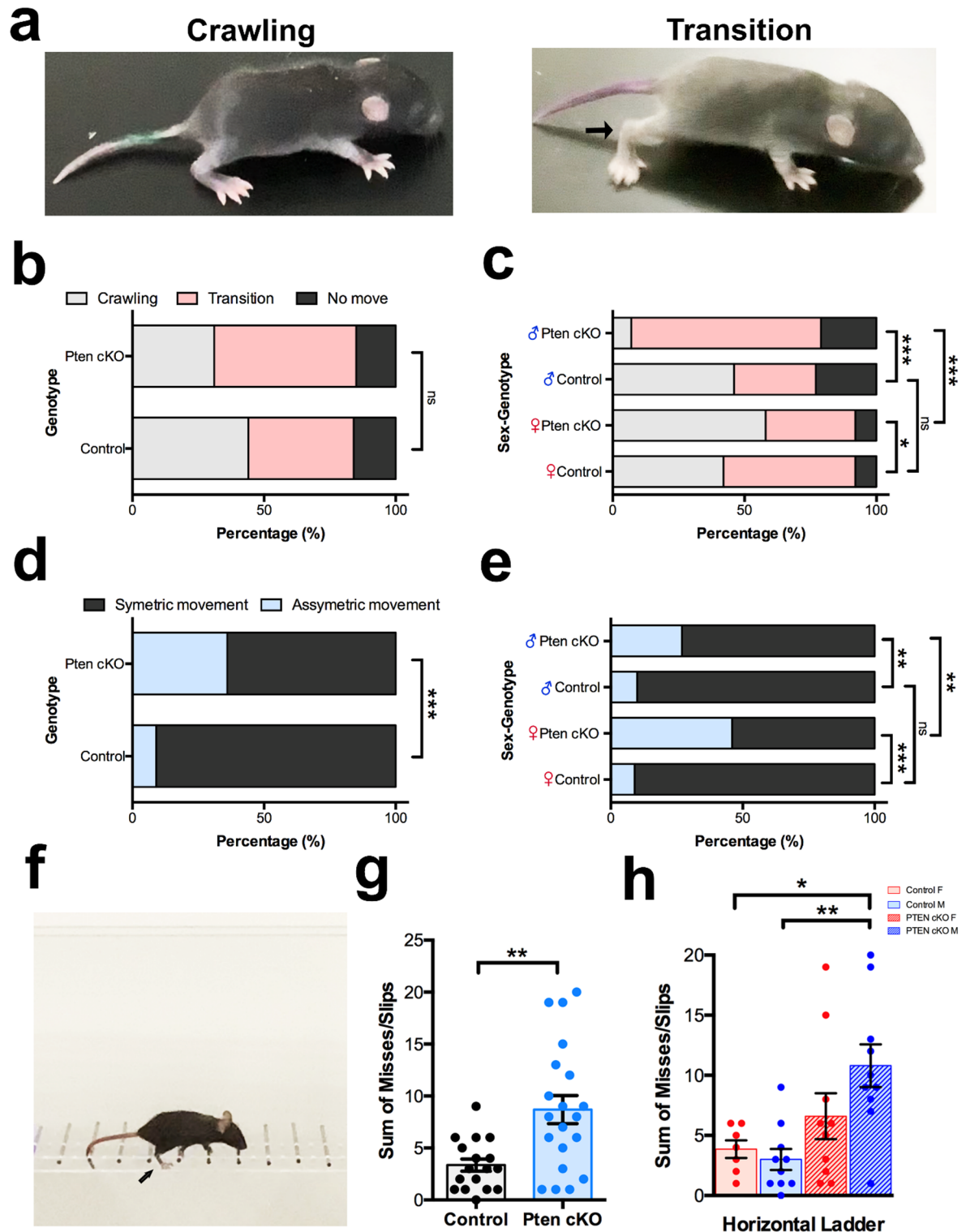


**Fig. 3.** Dendritic alterations in PCs and motor deficits in P30 *Pten* cKO mice. (a) Images of magnified dendritic branches from P30 Control and *Pten* cKO PCs stained with the Golgi-Cox technique showing dendritic segments and spines. Blue dotted square shows the fraction of the square occupied by dendritic segments as quantified in (c). (b) Quantification of the number of dendritic spines per  $\mu\text{m}$  in P30 Control and *Pten* cKO PCs ( $n=10$  dendrite segment/mouse). (c) Quantification of the percentage of area fraction occupied by dendritic branches (a) from P30 Control and *Pten* cKO PCs ( $n=7$  dendritic areas/mouse). (d) Calbindin, Neurofilament, and VGLUT2 immunoreactivity in P30 Control and *Pten* cKO PCs and ML. (e,f) Quantification of the neurofilament (e) and VGLUT2 (f) volume in the ML of P14 and P30 Control and *Pten* cKO mice. Data presented as mean  $\pm$  SEM,  $n=4$  mice, \* $P<0.05$ , \*\* $P<0.001$ , and \*\*\* $P<0.001$  by unpaired *t*-test. Scale bar: (a) 5  $\mu\text{m}$ , (d) 30  $\mu\text{m}$ . ML molecular layer, PCL Purkinje cell layer.



during crawling (Fig. 4a-b)<sup>35</sup>. The ambulation of the pups was also classified as symmetric or asymmetric limb movement. At P8, no significant differences were found between the percentages of mice crawling, transitioning to walking, or not moving when comparing *Pten* cKO pups with control pups (Fig. 4c). However, when the data were stratified by sex, significant differences emerged between control and *Pten* cKO pups within each sex group (Fig. 4d). In fact, a significant higher percentage of *Pten* cKO female pups (58%) were crawling when compared to control female pups (42%) (Fig. 4d). In the *Pten* cKO male group, a significant higher percentage of pups were transitioning to walking (72%) when compared to control male pups (31%) and *Pten* cKO females (34%) (Fig. 4d). The percentage of not moving pups was similar between females and males independent of genotype (Fig. 4d). Although, no significant differences were found between control females and control males, our results showed that ambulation was significantly different between *Pten* cKO females and *Pten* cKO males (Fig. 4d).

◀ **Fig. 4.** *Pten* deficiency in PCs affects neonatal motor development towards ambulation. (a) Image showing crawling as defined by whole back paw touching the ground while ambulating. (b) Image showing transition to walking as defined by elevation at the heel of the back paw (black arrow). (c) Percentage of mice in crawling, transition, or no movement ambulation categories by genotype (Control  $n=25$ ; *Pten* cKO  $n=26$ ). (d) Percentage of mice in Crawling, Transition, or No movement ambulation categories by sex/genotype (Control ♀  $n=12$ , ♂  $n=13$ ; *Pten* cKO ♀  $n=12$ , ♂  $n=14$ ). (e) Percentage of mice in Symmetric or Asymmetric ambulation movement by genotype (Control  $n=21$ ; *Pten* cKO  $n=22$ ). (f) Percentage of mice in Symmetric or Asymmetric ambulation movement by sex/genotype (Control ♀  $n=11$ , ♂  $n=10$ ; *Pten* cKO ♀  $n=11$ , ♂  $n=11$ ). \* $P<0.05$ , \*\* $P<0.001$ , and \*\*\* $P<0.001$ , by Fisher's exact test. (g) Image showing a *Pten* cKO mouse missing/slipping (arrow) a rung in the ladder rung task. (h) Quantification of the total number of misses/slips in the ladder rung task throughout 3 trials by P30 Control ( $n=17$  mice) and *Pten* cKO ( $n=20$  mice). Data presented as mean  $\pm$  SEM; \*\* $P<0.001$  by unpaired *t*-test. (i) Quantification of the total number of misses/slips in the ladder rung task by sex (Control mice: F  $n=7$ , M  $n=10$ ; *Pten* cKO mice: F  $n=10$ , M  $n=10$ ), data presented as mean  $\pm$  SEM, \* $P<0.05$  and \*\* $P<0.001$  by One-way ANOVA with post-hoc Tukey.

In terms of motor coordination, a significant larger percentage of pups in the *Pten* cKO group (36%) was found with asymmetric movement when compared to the control group (10%) (Fig. 4e). After segregating the data by sex, a significant larger percentage of *Pten* cKO female pups had asymmetric movement (46%) when compared to control female pups (9%) and *Pten* cKO males (27%) (Fig. 4f). It was also found that a significant higher percentage of *Pten* cKO male pups had asymmetric movement than control male pups (10%). Once again, no significant differences were found between control females and control males when assessing movement symmetry. These data demonstrate early sexually dimorphic motor behavior in *Pten* cKO mouse pups that is caused by the deficiency of PTEN specifically in PCs. Interestingly, similar to our results, in human ASD, higher motor scores are found in toddler males than in toddler females<sup>36</sup> mostly because preschooler ASD males are found to have better gross motor skills than preschooler ASD females<sup>37</sup> suggesting that ASD associated brain changes affect differently the motor function of males and females.

Motor coordination and balance was also altered in P30 *Pten* cKO mice, where the number of misses and slips in a ladder rung walking task were significantly higher in P30 *Pten* cKO mice, particularly in males, than in control mice (Fig. 4 g-i). This task is a fine motor performance test, suggesting that fine motor function is significantly affected in juvenile *Pten* cKO mice, but more severely in males. Studies in human ASD have also reported better fine motor function in females<sup>37</sup> once again suggesting that the impact of cerebellar changes in ASD motor function is differentially influenced by sex.

Early cerebellar injury in children has been associated with an increased risk of developing autistic behaviors<sup>21,38</sup> supporting the contribution of the cerebellum to human ASD. Since autistic traits were previously reported in adult *Pten* cKO male mice<sup>12</sup> we examined if social and non-social behaviors were altered in juvenile P21 *Pten* cKO mice using the “Juvenile Play” behavioral test as previously described<sup>39,40</sup>. For this test, individual control and *Pten* cKO mice were placed in a cage with an unfamiliar wild-type mouse. The behaviors and interactions of the control and *Pten* cKO mice with the unfamiliar mouse were analyzed. We found that the nose-to-nose interaction was significantly reduced in male and female *Pten* cKO mice when compared to male and female control mice respectively (Fig. 5a-b). *Pten* cKO male mice had significant less anogenital sniffing interaction than control female mice, but no differences were found between the other groups (Fig. 5c). The number of events for following and crawling under the unfamiliar mouse was similar between all the groups (Fig. 5a, d-e). In terms of non-social behaviors, wall rearing was significantly higher in *Pten* cKO females than *Pten* cKO males, but not different from control mice (Fig. 5f-g). It was also found that *Pten* cKO females were significantly more active exploring the cage than *Pten* cKO and control males (Fig. 5f and h). No significant differences were found in time sitting alone or self-grooming behaviors when comparing control and *Pten* cKO mice (Fig. 5i and j). Overall, these results suggest that at P21, nose-to-nose behavior is a social interaction affected by deficiency of *Pten* in PCs, while changes in certain non-social behaviors may suggest a grade of hyperactivity in *Pten* cKO females.

**PTEN deficiency in postnatal Purkinje cells alters mTOR pathway and dendritic mitochondria**  
 PTEN is a negative regulator of the mTOR pathway, therefore, aberrant hyperactivation of mTORC1 has been found in adult *Pten* cKO PCs<sup>12,41</sup>. As previously reported<sup>30</sup> P14 control PCs exhibited significantly higher levels of phosphorylated S6 ribosomal protein (pS6R), a downstream target of mTORC1/S6K signaling, compared to P30 control PCs (Fig. 6a-b), supporting a critical role for mTORC1 activity during early postnatal development. Interestingly, in *Pten* cKO mice, pS6R immunoreactivity was reduced in P14 PCs relative to their age-matched controls and was comparable to levels observed in P30 *Pten* cKO PCs (Fig. 6a-b). Still, pS6R intensity levels were higher in P30 *Pten* cKO PCs compared to control PCs (Fig. 6a-b). No differences in pS6R fluorescent immunoreactivity in the granule layer was found between genotypes (Fig. S2), confirming that PTEN deficiency induces these changes specifically in PCs.

However, since S6R protein can be phosphorylated by multiple kinases and is subject to regulation by phosphatases<sup>42</sup> we employed an antibody against phosphorylated mTOR at serine 2448. This phosphorylation site is commonly associated with the negative regulation of mTORC1 activity mediated by its downstream effector, S6K<sup>43,44</sup>. This approach allowed us to more directly investigate the presence of a negative feedback loop regulating mTOR activity in PTEN-deficient PCs at P14. In contrast to pS6R, phosphorylated mTOR (Ser2448) immunoreactivity was significantly elevated in PCs from *Pten* cKO mice compared to controls (Fig. 6c-d), suggesting that hyperactivation of the mTORC1/S6K pathway may trigger a negative feedback mechanism

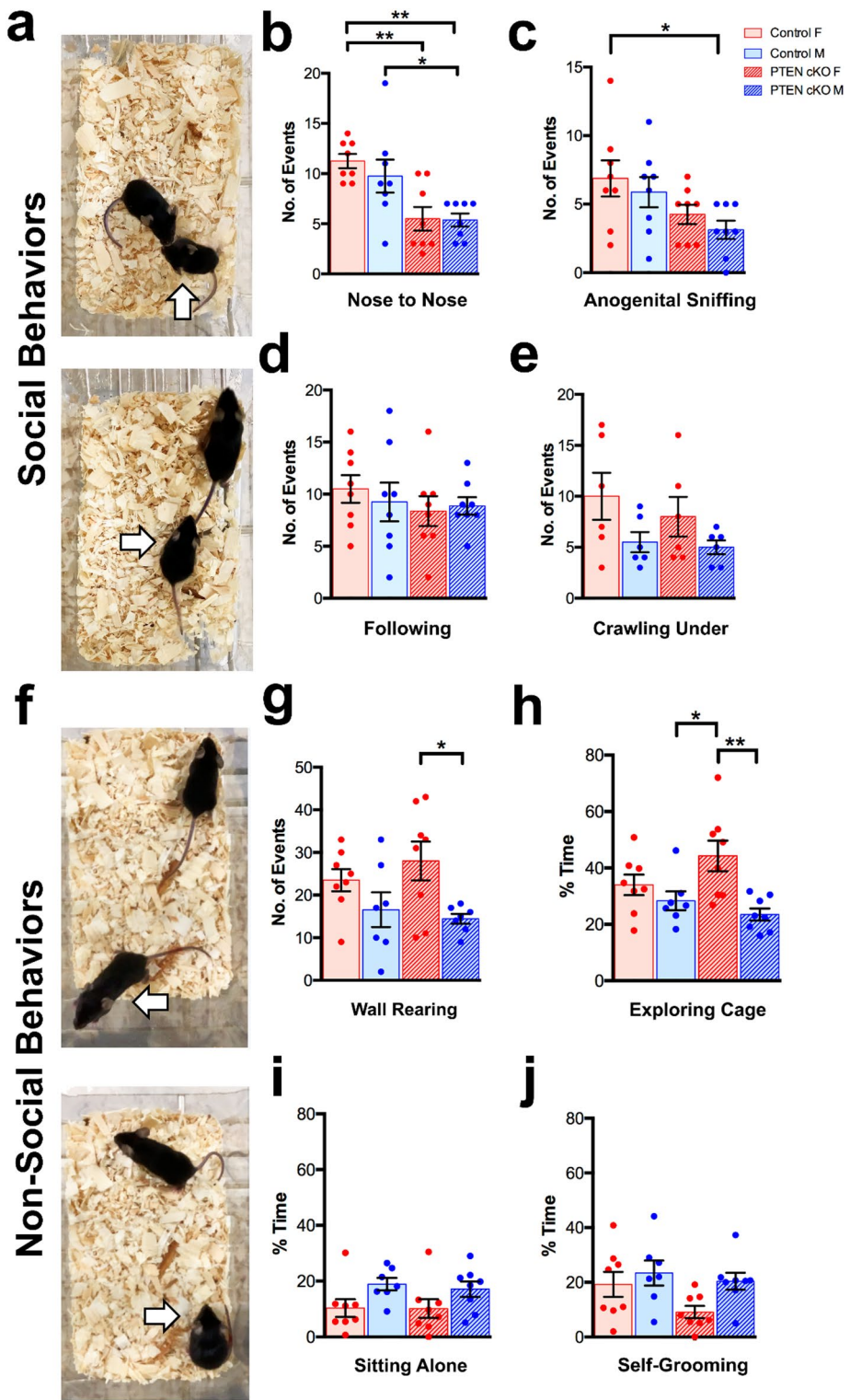


**Fig. 5.** Assessing social and non-social behaviors in P21 Control and *Pten* cKO mice by sex. (a) Images showing the social behaviors nose to nose interaction (top) and following (bottom); arrow indicates the analyzed mouse. (b–e) Quantifications of the number of events for the social behaviors nose-to-nose (b), anogenital sniffing (c), following (d) and crawling under (e) in P21 Control and *Pten* cKO mice by sex. Second mouse in the cage is with the Control and *Pten* cKO mouse is an unfamiliar wild-type mouse. (f) Images showing the non-social behaviors exploring the cage and wall rearing (top) and sitting alone (bottom); arrow indicates the analyzed mouse. (g–j) Quantifications of non-social behaviors including the number of wall rearing events (g) and the percentage of time exploring the cage (h), sitting alone (i) and self-grooming (j) in P21 Control and *Pten* cKO mice by sex. Data presented as mean  $\pm$  SEM,  $n=9$ –11 mice/genotype/sex. \* $P<0.05$ , \*\* $P<0.001$  by One-way ANOVA with post-hoc Tukey.

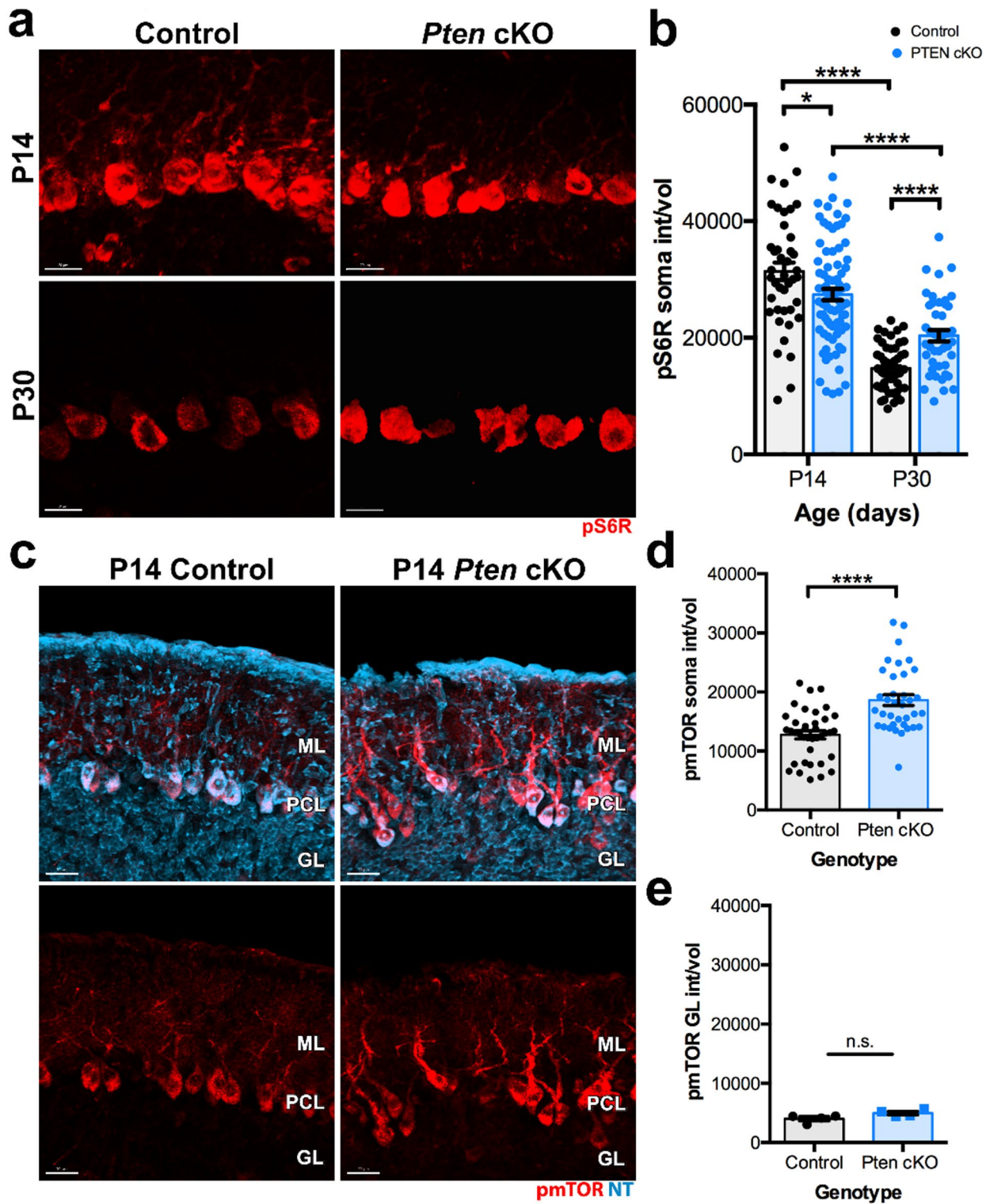


**Fig. 6.** Immunoreactivity of pS6 ribosomal protein and phosphorylated mTOR in control and *Pten* cKO PCs during postnatal development. (a) Images of pS6R immunoreactivity in PCs from control and *Pten* cKO mice at P14 and P30. (b) Quantification of the pS6R soma intensity per cell volume in control and *Pten* cKO PCs at P14 and P30. Data presented as mean  $\pm$  SEM,  $n = \sim 12$  cells/mouse from  $n = 5$ –7 mice (P14) and  $n = 4$  mice (P30). (c) Images of p-mTOR immunoreactivity in PCs from control and *Pten* cKO mice at P30. (d) Quantification of the p-mTOR soma intensity per NT cell volume in control and *Pten* cKO PCs at P14. (e) Quantification of the p-mTOR GL intensity per NT cell volume in control and *Pten* cKO PCs at P14. Data presented as mean  $\pm$  SEM,  $n = 8$ –10 cells/mouse from 4 mice. \* $P < 0.05$  and \*\*\*\* $P < 0.0001$  by unpaired *t*-test. Scale bar: (a) 20  $\mu$ m, (c) 30  $\mu$ m. ML molecular layer, PCL Purkinje cell layer, GL granular layer.

regulating mTOR activity. No differences in phosphorylated mTOR were observed in the granule cell layer between control and *Pten* cKO mice (Fig. 6c, e), indicating that these alterations are specific to PTEN-deficient PCs. These changes in mTORC1 signaling correlate with the observed differences in dendritic growth between control and *Pten* cKO mice at P14 and P30. Specifically, reduced pS6R and elevated p-mTOR (Ser2448) levels at P14 are associated with delayed dendritic growth, whereas increased pS6R expression at P30 corresponds with a partial recovery in dendritic complexity in *Pten* cKO PCs. Overall, these data suggest that after mTORC1 hyperactivation, S6K-mediated negative feedback on upstream signaling (including mTOR and AKT) could suppress growth in *Pten* cKO PCs. However, as negative feedback diminishes over time or time-dependent growth stimuli emerge, mTORC1 signaling may recover, allowing growth to resume.

It is also possible, that early overactivation of mTORC1 in PTEN-deficient PCs may induce metabolic stress or mitochondrial deficits that limit dendritic growth by P14. Given that the deregulation of mTORC1 causes neuronal mitochondria deficits<sup>30,45</sup>, we interrogated if lack of PTEN in PCs alters mitochondria during dendritic postnatal development. To determine mitochondria volume in PC dendrites, the ratio between the total volume of PDHE1<sup>+</sup> mitochondria and the total volume of CALB<sup>+</sup> PC dendrites was calculated as described previously<sup>30</sup>. Higher levels of PDHE1<sup>+</sup> mitochondria in PC dendrites were found in both control and *Pten* cKO mice at P14 when compared to P30 control mice (Fig. 7a-c, Fig. S3a-b). However, the levels of PDHE1<sup>+</sup> mitochondria in PC dendrites were significantly reduced in P14 *Pten* cKO mice compared to P14 control mice (Fig. 7a and c, Fig. S3a), but not significantly different than P30 *Pten* cKO mice (Fig. 7b and c, Fig. S3b). Knowing that mTORC1 regulates lysosomal biogenesis and function<sup>46</sup>, measure of the total volume of lysosomes in *Pten* cKO PC dendrites was determined by calculating the ratio between the total volume of LAMP1<sup>+</sup> lysosomes and the total volume of CALB<sup>+</sup> PC dendrites. At P14, *Pten* cKO mice have significantly lower total volume of LAMP1<sup>+</sup> lysosomes in CALB<sup>+</sup> PC dendrites than control mice (Fig. 7a and d, Fig. S3a). The total volume of LAMP1<sup>+</sup> lysosomes in CALB<sup>+</sup> PC dendrites was significantly decreased in P30 control mice when compared to P14 control mice, but similar to P30 *Pten* cKO mice. No differences in the total volume of PDHE1<sup>+</sup> mitochondria and LAMP1<sup>+</sup> lysosomes in CALB<sup>+</sup> PC cell bodies were found between control and *Pten* cKO mice at P14 and P30 (Fig. S3a-d). The total volume of PDHE1<sup>+</sup> mitochondria and LAMP1<sup>+</sup> lysosomes in CALB<sup>+</sup> PC dendrites were also remarkably reduced in the degenerating dendrites of PCs at 8 m in *Pten* cKO mice (Fig. S4). Although at P30 the levels of PDHE1<sup>+</sup> mitochondria in PC dendrites were similar between control and *Pten* cKO mice, cytochrome c oxidase (COX) histochemistry was significantly reduced in P30 *Pten* cKO ML when compared to control mice (Fig. S5), suggesting mitochondria activity deficits in *Pten* cKO PCs.

Mitochondrial deficits can lead to cellular energy stress, resulting in an elevated intracellular AMP-to-ATP ratio<sup>47,48</sup>. To restore ATP levels, LKB1 (Liver kinase B1) phosphorylates the AMPK protein, which inhibits mTORC1, activates catabolic processes, and increases mitochondria biogenesis<sup>48–50</sup>. AMP can also allosterically bind AMPK to directly activate this kinase<sup>51</sup>. Because we found reductions in the phosphorylation of S6R and dendritic mitochondria total volume in P14 *Pten* cKO PCs, we examined the activation of LKB1 and AMPK in control and *Pten* cKO PCs at P14. No significant differences in phosphorylated LKB1 (pLKB1) immunoreactivity were found in P14 *Pten* cKO PCs compared to P14 control PCs (Fig. 8a and c). However, phosphorylated AMPK (pAMPK) was significantly decreased in P14 *Pten* cKO PCs compared to P14 control PCs (Fig. 8b and d), suggesting that P14 *Pten* cKO PCs are unable to reach metabolic balance and restore mitochondria levels at this postnatal developmental stage. No significant differences in pLKB1 and pAMPK immunoreactivity were found in the granular layer of P14 control and *Pten* cKO mice (Fig. S6).

To investigate how manipulation of the AMPK and mTOR pathways influences the pathology of developing *Pten* cKO PCs, cerebellar organotypic slice cultures (COSCs) were employed. Control and *Pten* cKO cerebella were dissected at P11 (day in vitro 0, DIV0). At this stage, the pronounced increase in dendritic growth observed through Golgi-Cox analysis was further confirmed by the significant difference in molecular layer (ML) length between control and *Pten* cKO PCs (Fig. 9a-b). After 4 days in vitro (DIV4), the ML length in control PCs was significantly larger than control DIV0 PCs and DIV4 *Pten* cKO PCs. No significant differences in ML length were found in *Pten* cKO PCs at DIV4 when compared to DIV0 *Pten* cKO PCs (Fig. 9a-b), showing no further vertical growth after 4 DIV. We also measured the dendritic terminal points of CALB<sup>+</sup> dendrites at DIV4 and found no difference between control and *Pten* cKO PCs (Fig. 9c). At DIV0, when the *Pten* cKO PC dendrites are overgrown, pS6R was significantly increased in *Pten* cKO PCs compared to control PCs (Fig. 9d-e, dotted line), showing that mTORC1 is hyperactivated at this early postnatal developmental stage, coinciding with the overgrowth of dendrites found in P10 *Pten* cKO PCs.

AICAR, is an AMPK agonist that stimulates mitochondrial and lysosomal biogenesis in cultured cells including neurons<sup>52,53</sup>. COSCs from P11 *Pten* cKO mice were treated with AICAR or vehicle from DIV0 to DIV4. No changes in dendritic arborization were found, as the dendritic total length and number of terminal points were similar between vehicle and AICAR treated *Pten* cKO PCs (Fig. 10a-c). However, a significant increase in the dendritic total volume of PDHE1<sup>+</sup> mitochondria and LAMP1<sup>+</sup> lysosomes was found in AICAR treated *Pten* cKO PCs compared to vehicle treated *Pten* cKO PCs (Fig. 10a, d-e). Next, we used the drug Torin1 to inhibit mTOR hyperactivation in P10 *Pten* cKO COSCs from DIV0 to DIV4. This drug increases TFEB-induced lysosomal function<sup>53</sup>, prevent mitochondria fission during normal conditions<sup>54</sup> and ameliorate mitochondria pathogenesis during mTORC1 hyperactivation<sup>45</sup>. Torin1 significantly increased the dendritic number of terminal points but not the total dendritic length in DIV4 *Pten* cKO PCs when compared to vehicle treated DIV4 *Pten* cKO PCs (Fig. 10f-h). Torin1 also significantly increased the dendritic PDHE1<sup>+</sup> mitochondria total volume in DIV4 *Pten* cKO PCs, but not the dendritic total volume of LAMP1<sup>+</sup> lysosomes when compared to vehicle treated DIV4 *Pten* cKO PCs (Fig. 10f, i-j). These findings suggest that although both AICAR and Torin1 increase mitochondrial content in the dendrites of DIV4 *Pten* cKO PCs, only Torin1 promotes dendritic growth. This implies that AMPK activation alone may be insufficient to fully counteract the mTORC1/S6K pathway hyperactivation caused by PTEN deficiency. It remains to be determined whether AMPK activation or direct mTOR inhibition can also

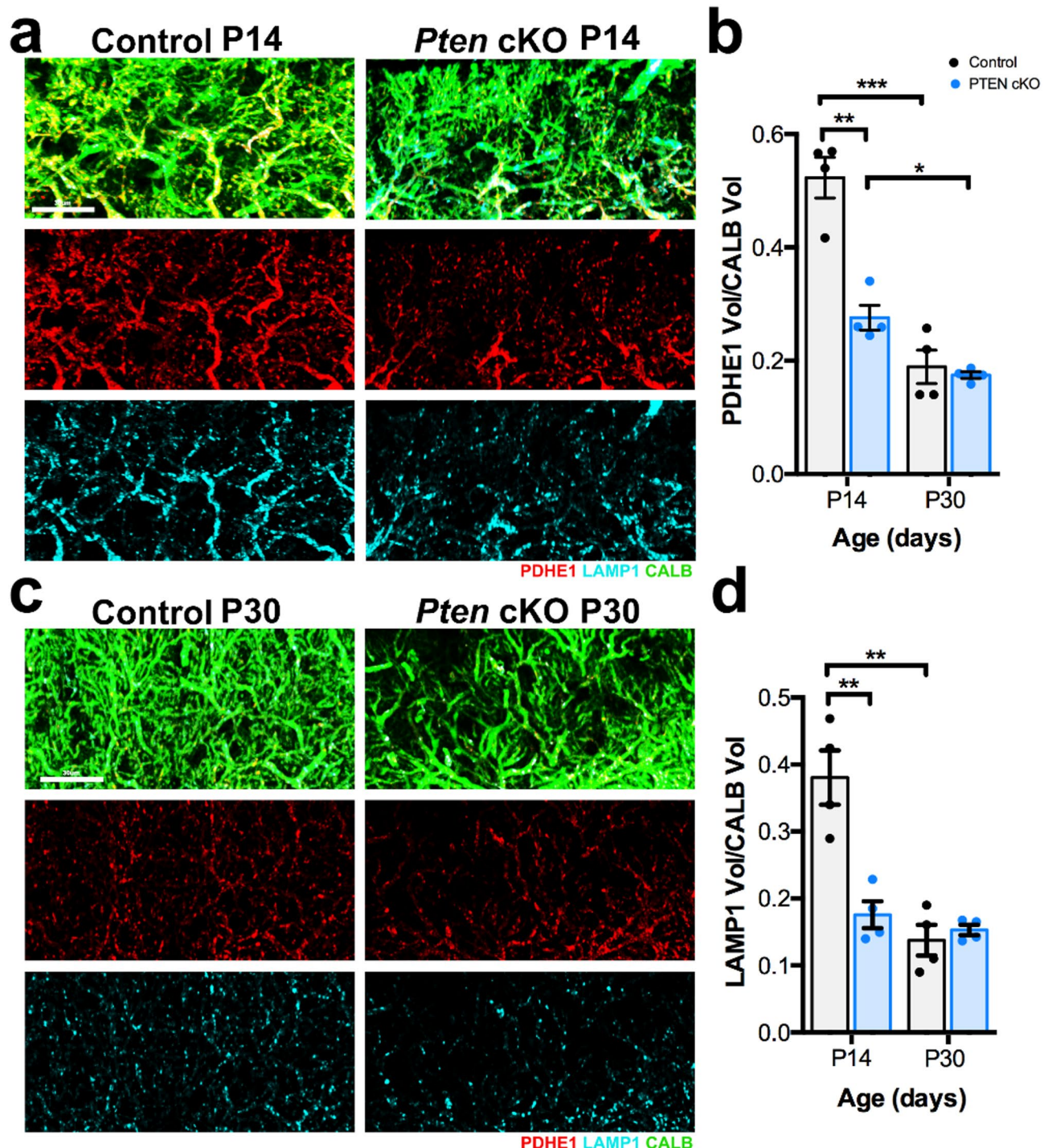


**Fig. 7.** *Pten* conditional deletion in PCs alters mitochondrial and lysosomal levels in PC dendrites during postnatal development. (a,b) Digitally segregated PDHE1 (mitochondria) and LAMP1 (lysosomes) immunoreactivity in CALB<sup>+</sup> PC dendrites in Control and *Pten* cKO mice at P14 (a) and P30 (b). (c) Quantification of the ratio between PDHE1<sup>+</sup> mitochondria volume and CALB<sup>+</sup> PCs' dendrites' volume at P14 and P30 in Control and *Pten* cKO mice. (d) Quantification of the ratio of LAMP1<sup>+</sup> lysosomes' volume and CALB<sup>+</sup> PCs' dendrites' in P14 (a) and P30 (b) Control and *Pten* cKO mice. Data are presented as mean±SEM,  $n=4$  mice/genotype/age, \* $P<0.05$ , \*\* $P<0.01$ , and \*\*\* $P<0.001$  by unpaired *t*-test. Scale bars: (a) 30  $\mu$ m.

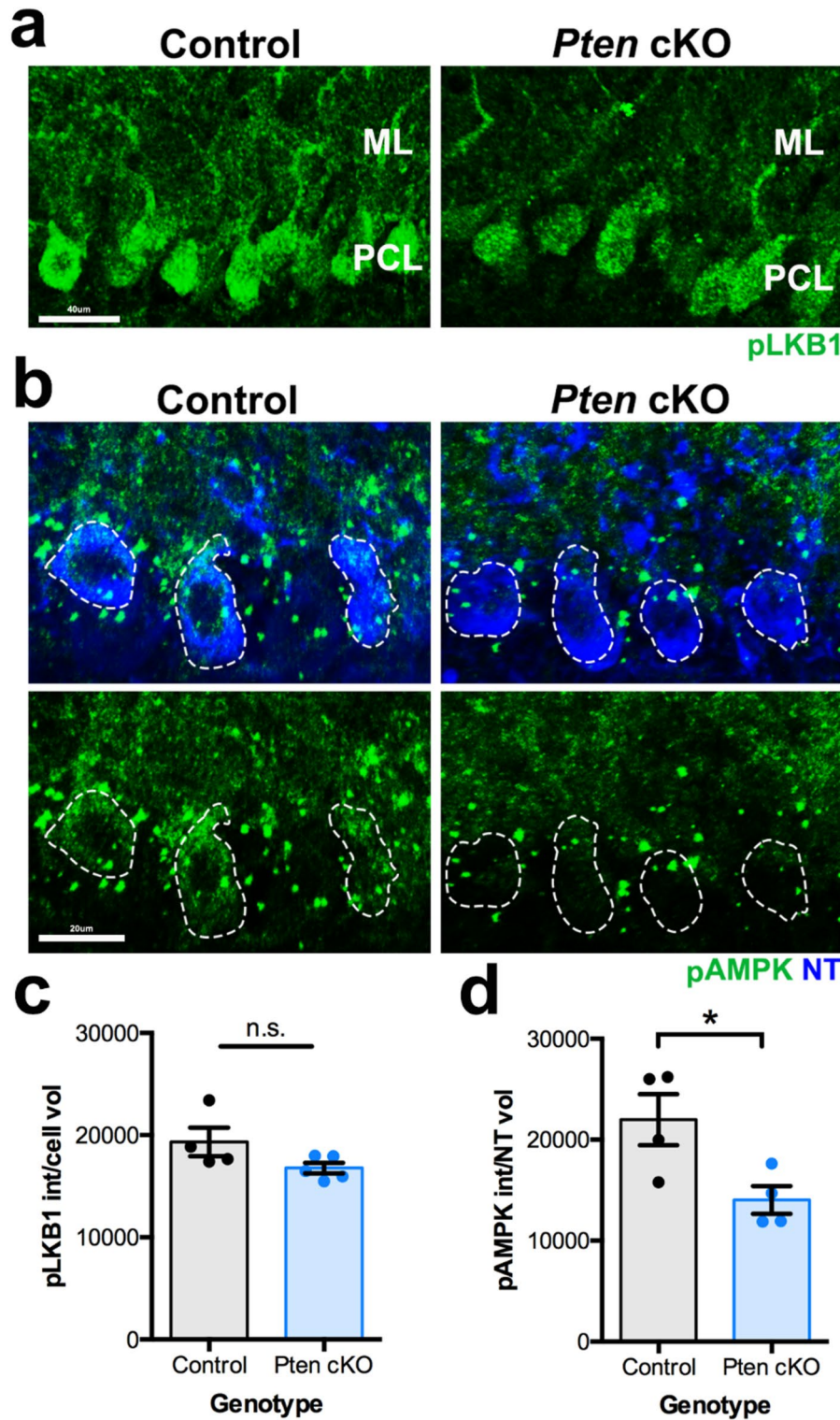


**Fig. 8.** Immunoreactivity of pLKB and pAMPK in P14 control and *Pten* cKO PCs. **(a)** Images of pLKB1 immunoreactivity in P14 PCs from control and *Pten* cKO mice. **(b)** Images of pAMPK immunoreactivity and NeuroTrace staining in P14 PCs from control and *Pten* cKO mice. **(c)** Quantification of the pLKB1 soma intensity per cell volume in control and *Pten* cKO PCs at P14. **(d)** Quantification of the pAMPK soma intensity per cell volume in control and *Pten* cKO PCs at P14. Data presented as mean $\pm$ SEM,  $n=4$  mice (8–10 cells/mouse),  $^*P<0.05$  by unpaired *t*-test. Scale bar: **(a)** 40  $\mu$ m, and **(b)** 20  $\mu$ m. **ML** molecular layer, **PCL** Purkinje cell layer.

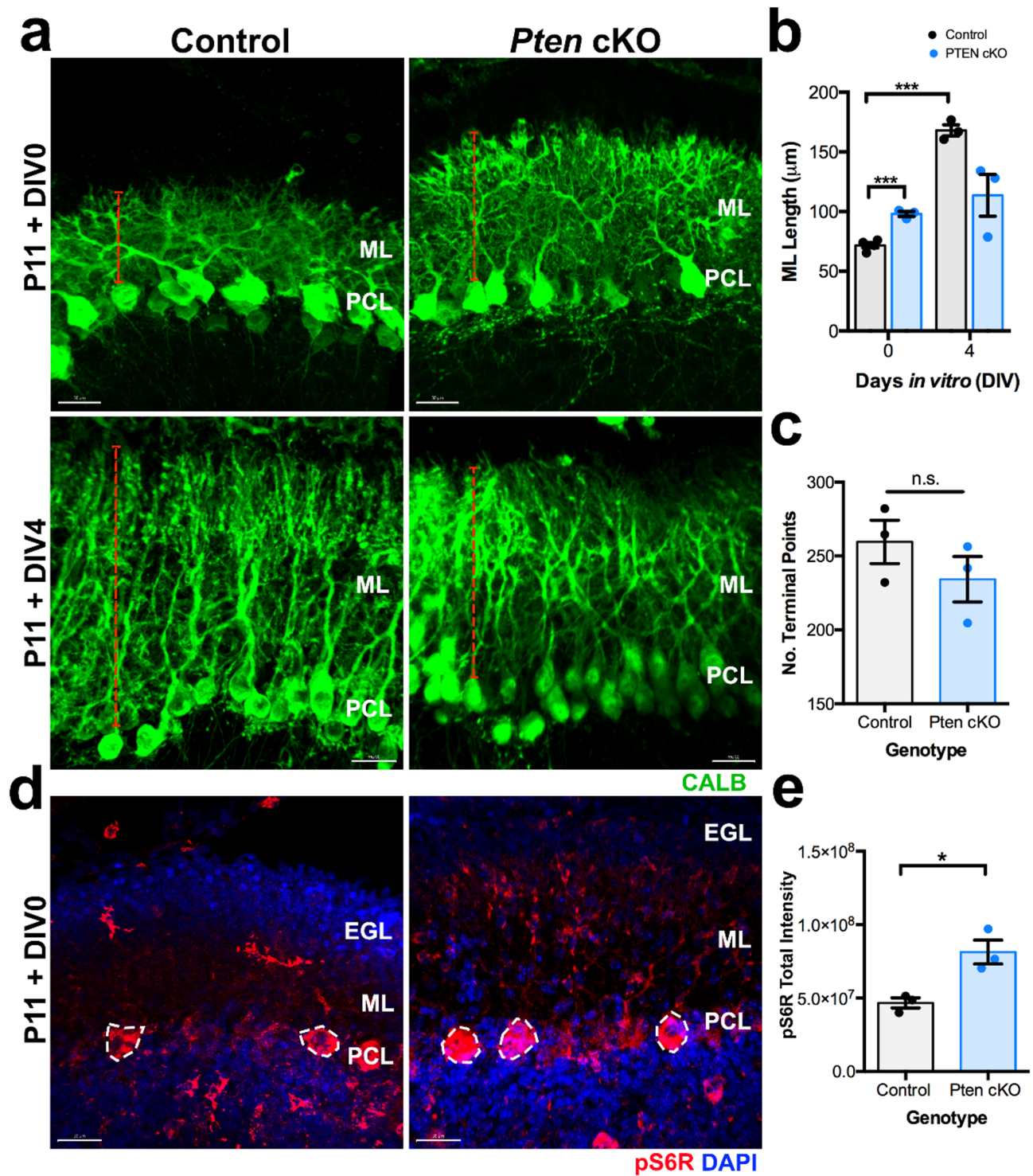
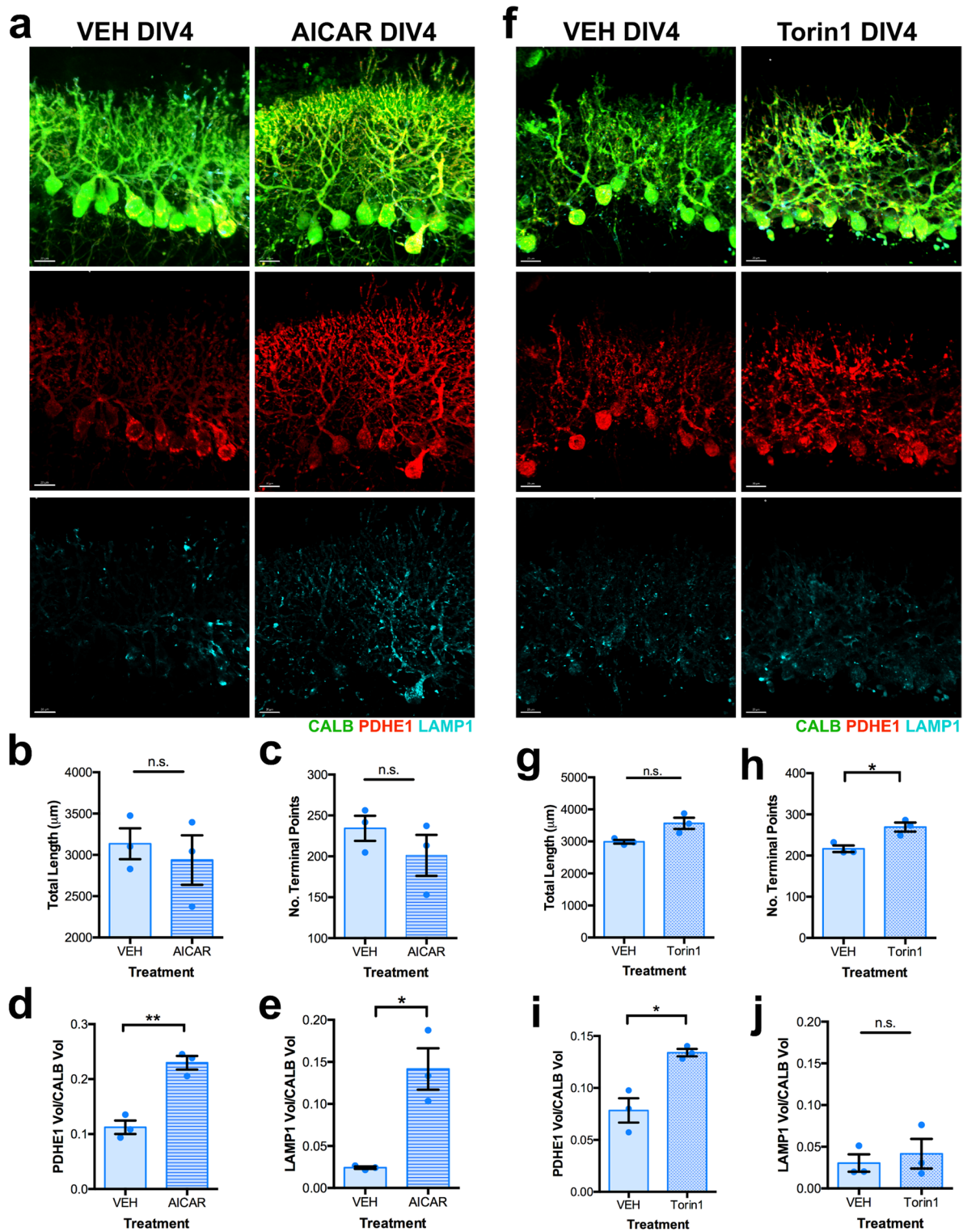


**Fig. 9.** Dendritic growth anomalies in postnatal *Pten* cKO PCs ex-vivo. (a) CALB<sup>+</sup> PCs from P11 Control and *Pten* cKO COSCs at DIV0 and DIV4 show differences in dendritic growth. Red dotted line shows ML length. (b) Quantification of ML length in DIV0 and DIV4 COSCs from P11 Control and *Pten* cKO mice. (c) Quantification of the number of dendritic terminal points in DIV0 and DIV4 COSCs from P11 Control and *Pten* cKO mice. (d) pS6 immunoreactivity in DIV0 COSCs from P11 Control and *Pten* cKO mice. (e) Quantitative analysis of the pS6 total intensity in PCs from P11 + DIV0 Control and *Pten* cKO mice. Data are presented as mean $\pm$ SEM,  $n=3$  mice/genotype/age. \* $P < 0.05$  and \*\*\* $P < 0.001$  by unpaired *t*-test. Scale bars: (a) and (d) 30  $\mu$ m. ML molecular layer, PCL Purkinje cell layer, EGL external granule layer.



mitigate other pathological features observed in *Pten* cKO PCs, such as neurofilament accumulation, dendritic thickening, and synapse loss.

## Discussion

Heterozygous PTEN mutations have been linked to ASD cases of macrocephaly, a phenotype also common in idiopathic ASD<sup>55–57</sup> and thought to result from early brain overgrowth. Consistent with previous findings in adult male mice<sup>12</sup> we observed PC dendritic swelling and degeneration in the cerebellar molecular layer of both male and female adult *Pten* cKO mice. Given PTEN's association with neurodevelopmental disorders, we examined its role in postnatal PC development. We found that PTEN deficiency disrupted dendritic growth and structure, leading to cytoskeletal abnormalities, dendritic thickening, and synapse loss. These alterations significantly impaired motor function in early postnatal stages and mildly affected behavior in juveniles. Additionally, PTEN

**Fig. 10.** Effects of AICAR and Torin1 treatments in *Pten* cKO PCs ex-vivo. (a) Vehicle and AICAR treated *Pten* cKO PCs from P11 COSCs cultured for 4 DIV immunolabeled with CALB, PDHE1, and LAMP1. (b) Quantitative analysis of the dendritic total length of P11 + DIV4 CALB<sup>+</sup> PCs in vehicle and AICAR treated *Pten* cKO COSCs. (c) Quantitative analysis of the total number of dendritic terminal points in P11 + DIV4 CALB<sup>+</sup> PCs from vehicle and AICAR treated *Pten* cKO COSCs. (d) Quantitative analysis of PDHE1<sup>+</sup> mitochondria total volume in PC dendrites from vehicle and AICAR treated P11 + 4DIV COSCs. (e) Quantitative analysis of LAMP1<sup>+</sup> lysosomes' total volume in PC dendrites from vehicle and AICAR treated P11 + 4DIV COSCs. (f) Vehicle and Torin1 treated *Pten* cKO PCs from P10 COSCs cultured for 4 DIV immunolabeled with CALB, PDHE1, and LAMP1. (g) Quantitative analysis of the dendritic total length of P10 + DIV4 CALB<sup>+</sup> PCs in vehicle and Torin1 treated *Pten* cKO COSCs. (h) Quantitative analysis of the total number of dendritic terminal points in P10 + DIV4 CALB<sup>+</sup> PCs from vehicle and Torin1 treated *Pten* cKO COSCs. (i) Quantitative analysis of PDHE1<sup>+</sup> mitochondria total volume in PC dendrites from vehicle and Torin1 treated P10 + 4DIV COSCs. (j) Quantitative analysis of LAMP1<sup>+</sup> lysosomes' total volume in PC dendrites from vehicle and Torin1 treated P10 + 4DIV COSCs. Data are presented as mean  $\pm$  SEM,  $n=3$  mice. \* $P < 0.05$  and \*\* $P < 0.001$  by unpaired *t*-test. Scale bar: (a) and (f) 20  $\mu$ m.

loss dysregulated mTOR and AMPK signaling, resulting in mitochondrial and lysosomal deficits in dendrites, suggesting that disrupted metabolic signaling contributes to dendritic pathology in *Pten* cKO PCs.

PC dendritic development in rodents follows eight distinct phases. During phase 6 (P9–P10), dendrites extend vertically and begin branching; in phase 7 (P10–P14), growth shifts laterally; and in phase 8 (P15–P21), vertical extension resumes<sup>58,59</sup>. These changes likely reflect coordinated intrinsic programs modulated by environmental cues such as nutrients, hormones, and neurotrophins. In PTEN-deficient PCs, we observed premature dendritic overgrowth at P10, which stalled by P14, suggesting a disruption in normal developmental pacing. Interestingly, by P30, dendritic growth recovered to control levels, possibly in response to a late developmental stimulus. Remarkably, cerebellar expression of brain-derived neurotrophic factor (BDNF), a known activator of PI3K/AKT, ERK1/2, and mTORC1 signaling, rises after P15 and peaks at P30<sup>60–63</sup>, coinciding with the vertical dendritic extension characteristic of developmental phase 8. In cortical neurons, BDNF signaling activates mTOR activity and promote dendritic growth<sup>64</sup> suggesting that BDNF may help resume dendritic PC dendritic growth in *Pten* cKO PCs via mTORC1 activation.

Although dendritic growth and arborization appeared to reach control levels by P30 in *Pten* cKO mice, persistent thickening of dendritic branches and a reduction in spine density suggest ongoing dendritic dysfunction. These early pathological changes correlated with markedly elevated levels of neurofilaments in PC dendrites. Similar accumulations of other cytoskeletal proteins, including MAP2 and Tau, have also been observed in adult *Pten* cKO mice<sup>12,65</sup> where they are associated with dystrophic dendritic morphology and PC degeneration. Neurofilament aggregation is a common feature of neurodegenerative conditions and has been linked to their hyperphosphorylation<sup>66</sup> a phenomenon also observed in the *Pten* cKO model<sup>12,65</sup>. Notably, this hyperphosphorylation is driven by activation of Cdk5 and pERK1/2 signaling pathways<sup>65</sup> suggesting that PTEN deficiency may disrupt other intracellular signaling cascades. Furthermore, these dystrophic dendrites exhibited significant reductions in both dendritic spines and climbing fiber presynaptic terminal innervations. Given PTEN's established role in synaptogenesis<sup>33</sup> these findings highlight the need for further investigation into how cytoskeletal protein aggregation in *Pten* cKO PCs occurs and how impairs postnatal synaptic structure and function. Since PC loss is a hallmark of certain forms of ASD<sup>21</sup> uncovering the mechanisms underlying neurofilament aggregation may reveal novel therapeutic strategies to prevent or slow the progression of PC degeneration in ASD.

Motor deficits and cerebellar dysfunction are well-documented in ASD<sup>14–16,67–69</sup>. Individuals with PTEN-ASD frequently exhibit not only cognitive and social impairments but also motor coordination deficits<sup>70,71</sup>. Early motor delays have been proposed as potential early indicators of ASD<sup>72,73</sup> with studies noting a link between motor and social development<sup>74</sup>. Although atypical motor function is common in ASD<sup>67,75</sup> its developmental trajectory remains unclear. In our study, *Pten* cKO pups displayed sex-dependent motor differences as early as P8. More *Pten* cKO males were transitioning to walking compared to controls and *Pten* cKO females, while a greater proportion of *Pten* cKO females exhibited asymmetric movements. These findings suggest that *Pten* cKO males exhibit accelerated motor and cellular development, whereas *Pten* cKO females show more pronounced motor impairments despite early dendritic overgrowth. This mirrors clinical observations that gross motor function tends to be more affected in females than males with ASD<sup>36,37</sup>.

In contrast, fine motor deficits at P30 were more pronounced in male *Pten* cKO mice compared to both control and female *Pten* cKO mice. This aligns with clinical findings in ASD, where females often show greater improvement in fine motor skills over time than males<sup>37,76</sup>. These results suggest that the cerebellum, which is essential for coordinating and fine-tuning both gross and fine motor skills, may contribute to the observed motor impairments. Acting as the brain's "error correction" system, the cerebellum ensures smooth, precise, and well-timed movements by integrating sensory feedback to guide motor learning<sup>21,77,78</sup>. Due to limited sample sizes, we could not assess sex-specific differences in dendritic pathology; future studies are needed to explore how ASD-associated mutations interact with sex to influence neuronal development and motor behavior across the lifespan.

Given reports that *Pten* deficiency in PCs causes the presentation of autistic social and non-social traits in adult male mice<sup>12</sup> and that we found alterations of dendritic development in *Pten* cKO PCs, we next examined social and non-social behaviors in P21 mice. For social behaviors, we found that only the nose-to-nose sniffing behavior was significantly lower in *Pten* cKO mice (both sexes) compared to control mice, indicating that at this

early stage, changes in social behavior were subtle or at a starting point, but still detectable. Regarding non-social behaviors, significant differences were mostly found between *Pten* cKO females and males. *Pten* cKO females were more hyperactively exploring and rearing the cage walls than *Pten* cKO males, even when repetitive upright wall scrabbling/jumping behavior is found in adult *Pten* cKO males<sup>12</sup>. Self-grooming, which is significantly decreased in adult *Pten* cKO males compared to adult control males<sup>12</sup>, was not significantly different in P21 *Pten* cKO mice. Nevertheless, at this early stage, some significant differences can be observed between females and males in the *Pten* cKO group, suggesting that changes in behavior are driven by sex and age.

mTORC1 integrates signals from nutrients, growth factors, and energy status to promote anabolic processes and suppress catabolic ones. As a negative regulator of the PI3K/AKT/mTOR pathway, PTEN is critical for maintaining this metabolic balance. In postnatal *Pten* cKO PC, mTORC1 hyperactivation was associated with early dendritic overgrowth and dystrophy. Since mitochondrial biogenesis relies on lysosomal degradation of damaged mitochondria, excessive mTORC1 activity likely impairs lysosomal biogenesis and mitochondrial turnover, contributing to energy decline<sup>45,79–81</sup>. Consistent with this, we observed reduced mitochondrial volume and activity, as well as a significant loss of lysosomes in *Pten* cKO dendrites. Notably, mitochondrial levels were unchanged in PC somas, suggesting that PTEN deficiency may also disrupt dendritic mitochondrial trafficking. Similar metabolic and lysosomal deficits have been reported in models of Niemann-Pick Type C disease<sup>30,45</sup> where mTORC1 is hyperactivated, highlighting the particular vulnerability of PCs to impaired mitochondrial homeostasis.

PTEN promotes mitochondrial biogenesis through the AKT/GSK-3β/PGC-1α pathway<sup>7</sup>. In *Pten* cKO PC, loss of PTEN and reduced AMPK activity likely contribute to metabolic stress that impairs dendritic development. We propose that the early dendritic overgrowth observed at P10, driven by mTOR hyperactivation, was not sustained between P10 and P14 due in part to mitochondrial deficits. Notably, the recovery of dendritic growth between P14 and P30 coincides with a developmental increase in BDNF expression<sup>62,63</sup>. BDNF can independently promote mitochondrial biogenesis via MAPK and CREB-mediated activation of PGC-1α, potentially compensating for impaired PTEN/mTOR signaling during this later stage. Further research is needed to clarify BDNF's role in restoring dendritic growth in *Pten*-deficient PCs.

Although activation of the LKB1-AMPK pathway is typically expected in response to energy deficits, it was not observed in P14 *Pten* cKO PC, likely due to AKT and mTORC1-mediated suppression of AMPK<sup>49,50,82,83</sup>. Pharmacological activation of AMPK with AICAR restored mitochondrial and lysosomal levels in dendrites but did not enhance dendritic growth. In contrast, mTOR inhibition with Torin1 increased mitochondrial content and promoted dendritic growth, though lysosomal levels remained unchanged, likely due to persistent AKT inhibition of TFEB<sup>84</sup>. These results suggest that while both interventions can partially restore metabolic deficits in PTEN-deficient PCs, their ability to rescue dendritic structural changes and synaptic integrity remains unclear. Clinically, mTOR inhibition with everolimus has shown modest cognitive and behavioral benefits in individuals with PTEN-ASD, while AMPK activation has demonstrated therapeutic potential in other neurodevelopmental disorder models, including Fragile X and Rett syndromes<sup>85–87</sup>, suggesting that AMPK activation may be beneficial for PTEN-ASD. Further studies are needed to evaluate the developmental impact of AMPK-targeted therapies in PTEN deficiency. Overall, our study advances the understanding of how disruptions in metabolic signaling contribute to the pathological changes observed in neurodevelopmental disorders such as ASD and highlights potential therapeutic targets to mitigate disease progression.

## Methods

### Animals

All experiments involving mice were conducted in accordance with policies and procedures described in the Guide for the Care and Use of Laboratory Animals of the National Institutes of Health and were approved by the Animal Care and Use Committees at Providence College. The results and experiments of this study involving animals are also reported in accordance with ARRIVE guidelines. To study changes in mouse PCs dendrites during postnatal development caused by deficiency of *Pten*, the *Pten*<sup>fl/fl</sup> mouse strain (B6.129S4-*Pten*<sup>tm1Hwu</sup>/J, Jackson stock number 006440, The Jackson Laboratory) was crossed to the *Pcp2*-cre strain (B6.129-Tg(*Pcp2*-cre)2Mpin/J, Jackson stock number 004146, The Jackson Laboratory) to generate F1 heterozygous mice for both genes *Pten*<sup>fl/fl</sup>/*Pcp2*-Cre<sup>+/−</sup>. Then these doubled heterozygous mice were crossed to generate F2 mice homozygous for *Pten* and homozygous, heterozygous, or negative for *Pcp2*-Cre (*Pten*<sup>fl/fl</sup>/*Pcp2*-Cre<sup>+/+</sup>, *Pten*<sup>fl/fl</sup>/*Pcp2*-Cre<sup>+/−</sup>, *Pten*<sup>fl/fl</sup>/*Pcp2*-Cre<sup>−/−</sup>). These F2 mice were then used as breeders or experimental mice. Mice that were negative for *Cre* (*Pten*<sup>fl/fl</sup>/*Pcp2*-Cre<sup>−/−</sup>) were used as Control mice or to produce more Control mice. Both males and females were used in this study, at a ratio of 2:2 when 4 mice were used (wet lab experiments). For motor and behavioral tests between 9 and 14 mice were used per genotype/sex to be able to analyze sex effect.

Due to the inability to differentiate between homozygous and heterozygous *Pcp2*-Cre mice via PCR genotyping, both genotypes (*Pten*<sup>fl/fl</sup>/*Pcp2*-Cre<sup>+/+</sup> or *Pten*<sup>fl/fl</sup>/*Pcp2*-Cre<sup>+/−</sup>) were utilized as breeders. This breeding strategy resulted in a reduced occurrence of *Cre*-negative pups within these litters. To supplement the number of control mice, mating pairs of *Cre*-negative/ *Pten*<sup>fl/fl</sup> siblings (from *Cre*-positive mice) were established.

### Cerebellar tissue regional analysis

Previous research utilizing the *Pten*<sup>fl/fl</sup>/*Pcp2*-Cre<sup>−/−</sup> mouse model compared PC soma size and PC density between the anterior IV-V lobules and the posterior IX lobule<sup>12</sup>. Both regions exhibited a similar increase in soma size at 1, 2, 4, 6, and 9 months of age, as well as a similar reduction in PC density at 6 and 9 months. Importantly, in healthy mice, no significant differences in the spatiotemporal development of PC dendrites—such as dendritic complexity or molecular layer thickness—between the anterior (I/II/IIi) and posterior (IX/X)

lobes prior to three weeks of age<sup>88</sup>. As such, for our cerebellar tissue analyses described below, anterior and posterior lobes were sampled, particularly regions between the lobules IV/V and VIII, except for the Golgi Cox technique where the number of viable cells per section is very limited, in this case all regions of the cerebellum were sampled.

### Golgi-Cox staining technique

The Golgi-Cox staining technique was performed as described previously<sup>30</sup> using and following the instructions of a commercially available kit (FD Rapid GolgiStain™ Kit, FD NeuroTechnologies Inc.) Briefly, mice were euthanized with CO<sub>2</sub>, and brains were dissected and immersed in the impregnating solution (mixed solution A and b). Following two weeks incubation, mouse brains were rinsed and incubated in 20% sucrose and 15% glycerol for 72 h<sup>89</sup>. Next, brains were removed from the solution, quick-froze, and stored at -80 °C. After freezing the brains in optimal compound temperature (OCT) media, 150 µm cryostat sections were collected in solution C, followed by rinse water washes and immersion in the developing solution (solutions D and e). After mounting the sections on slides, the dried sections were dehydrated using 75%, 95%, and 100% ethanol prior to being immersed in Histo-Clear II (National Diagnostics). Slides were mounted using Permount and allowed to dry overnight prior to analysis. For this experiment, we used 4 P10 control mice from 3 different litters, 4 P10 *Pten* cKO mice from 2 different litters, 5 P14 control mice from 3 different litters, 6 P14 *Pten* cKO mice from 5 different litters, 4 P30 control mice from 2 different litters, and 4 P30 *Pten* cKO mice from 2 different litters.

### Mouse perfusion and tissue preparation

After euthanizing the mice with CO<sub>2</sub>, transcardial perfusion was performed using 1× PBS followed by 4% paraformaldehyde. The brains were then carefully dissected and fixed by immersion in 4% paraformaldehyde overnight. Following fixation, the brains were rinsed in 1× PBS, immersed in a 30% sucrose/PBS solution overnight at 4 °C, frozen in OCT, and cryosectioned into 40 µm and 50 µm floating sections.

### Immunohistochemistry

Immunofluorescence experiments were performed as previously described<sup>30</sup>. Floating sections (40–50 µm) were collected in 1× PBS, rinsed once in 1× PBT (PBS + 1% Triton X-100), and incubated overnight at 4 °C in a cocktail of primary antibodies diluted in 1× PBT with 20% normal donkey serum. After overnight incubation, the sections were rinsed three times with 1× PBT for 10 min each and then incubated for 1.5 h with the appropriate secondary antibodies (1:500, Jackson ImmunoResearch or Invitrogen). Cerebellar sections were subsequently washed three times with 1× PBT for 10–15 min, incubated with DAPI, and mounted in Poly-Aquamount (Polysciences).

The following primary antibodies were used: mouse anti-CALB (calbindin, 1:200, Sigma-Aldrich, #C9848), rabbit anti-IBA1 (1:200, Wako, #019-19741), rabbit anti-phosphorylated S6R (1:200, Cell Signaling, #4858), rabbit anti-phosphorylated mTOR (Ser 2448) (1:200, Cell Signaling, #2971), rabbit anti-pyruvate dehydrogenase E1 alpha (PDEH1) (1:200, GeneTex, #GTX104015), and rat anti-CD107a (LAMP-1) (1:200, BioLegend, #121602), rabbit anti-PTEN (1:200, Cell signaling, #9188), guineapig anti-VGLUT2 (1:200, Synaptic Systems, #135 404), mouse anti-neurofilament (1:200, BioLegend, # 837801), mouse anti-MAP2 (1:200, Sigma-Aldrich, MAB3418), rabbit anti-pAMPK (1:200, Cell Signalling, #4060), rabbit anti-pLKB1 (1:200, #3482) and NeuroTrace (Invitrogen).

### Cytochrome c oxidase (COX) histochemistry

COX activity in the ML of P30 Control and *Pten* cKO cerebella was assessed using the VitroView™ COX-SDH Double Histochemistry Stain Kit. The instructions of the kit were followed for the COX staining, but 30 µm cryostat sections were used. For the quantitative analysis, 40X images were taken using the Keyence BZ-X800 imaging system. The images were cropped 100 µm X 100 µm and the fraction area occupied by the COX staining was calculated using ImageJ by measuring the area threshold of the staining, which was inverted to white color in order to be selected by the threshold.

### Microscopy image analysis

For all the image analyses described below, investigators were blind to the mice genotype. All the images analyzed by the Bitplane Imaris™ software were acquired using the Zeiss LSM 700 laser scanning confocal microscope. Confocal image stacks were acquired using a 40× objective lens with a 1 µm interval through a 40 µm z-depth of the tissue. Two to three confocal images per mouse were taken in the cerebellar cortex.

To quantify the number of IBA1<sup>+</sup> microglia in the cerebellar molecular layer (ML) of 8 m Control and *Pten* cKO mice, 40X confocal images were cropped to 400 µm X 350 µm using the Imaris software. Manual quantifications of the cells were performed using the Cell Counter plugin from the ImageJ software. N=4 mice, 5 to 6 images per mouse.

For 3D image reconstructions and analyses, three sagittal 50 µm cerebellar sections were immunoreactive by free-floating immunohistochemistry. Confocal images and Imaris™ surface rendering tool were used to measure the total intensity levels of pS6R, p-mTOR, pLKB1, and pAMPK in individual PCs and granule cell layer (as internal control). NeuroTrace was used to label the PC soma when p-mTOR, pLKB, and pAMPK antibodies were used because of the weak signal of these antibodies. The values reported are the calculation of each cell total intensity by their soma volume calculated for pS6R or NT (p-mTOR, pLKB1 and pAMPK). For quantification of NF and VGLUT2 immunoreactivity, 40×3D confocal images were used to crop a region of the ML (300 µm height × 500 µm wide, z=20 µm), then using the Imaris™ software, a 3D surface rendering was made for the NF or VGLUT2 fluorescence that was used to obtain the sum of the volume of the NF or VGLUT2 immunolabeling in PC dendrites.

To quantify the total volume of PDHE1 and LAMP1 inside CALB<sup>+</sup> dendrites, a region in the ML (300  $\mu\text{m}$  height  $\times$  400  $\mu\text{m}$  wide) in 40 $\times$  confocal images was cropped and used to create a 3D surface rendering for CALB. The surface rendering was used to obtain the total sum of the volume of the CALB<sup>+</sup> dendrites. Then, the “Mask all” tool was used to create a new channel for the PDHE1<sup>+</sup> or LAMP1<sup>+</sup> fluorescence that is inside of the CALB created surface by clearing all the fluorescence that is not found overlapping/contacting the rendering surface. Then, 3D surface renderings were created for the newly created PDHE1 and LAMP1 channels in order to determine the volume of this staining that was inside the CALB<sup>+</sup> dendrites. The same procedure was used for the quantitative analysis of cell bodies, but by creating surface renderings for individual PC somas. The Imaris™ software calculated and provided the measurements of the respective volumes for PDHE1 and LAMP1, and the ratio of these markers in PC dendrites or somas were calculated by dividing them by the CALB volume of the dendrites or somas.

PCs stained by the Golgi-Cox technique were imaged with a Keyence BZ-X800 imaging system using the 40X objective (dendritic tracing) or 60X objective (dendritic spines counts) and the Quick Full Focus tool. The Simple Neurite Tracer plugin from the ImageJ software was used to trace the dendritic tree of Golgi-Cox-stained PCs and measure the total length and the total number of intersections (branching) by the distance from the soma using the Sholl-Analysis. For the quantification of Golgi-Cox-stained dendritic spines, the length ( $\mu\text{m}$ ) of dendritic processes without intersections was measured by drawing a line over the segment, then spines in that segment were manually counted (Cell counter plugin) using the ImageJ software. The number of spines per  $\mu\text{m}$  of each segment was calculated and reported in Fig. 6B graph. Two to three images were taken per mouse ( $n=4$  mice, Control  $n=53$  and *Pten* cKO  $n=60$  segments).

### Cerebellar organotypic slice culture

The culturing of cerebellar organotypic slices was performed as previously described<sup>90</sup>. Briefly, after euthanasia, postnatal mouse brains at day 10 (P10) or P11 were dissected and kept in cold HBSS. Then, the cerebellum was separated from the rest of the brain and the portion of the brain stem along with the meninges were carefully removed while keeping the tissue immersed in HBSS. Using a tissue slicer (Stoelting), 250  $\mu\text{m}$  slices were cut and plated on a membrane filter (Millicell-hydrophilic PTFE 0.4  $\mu\text{m}$ ; Millipore) coated with rat-tail collagen and immersed in slice medium (50% MEM, 25% horse serum (Invitrogen), 25% HBSS, 3mM GlutaMAX (Invitrogen), and 5 mg/ml glucose). The slices were cultured for 4 days at 37 °C in an environment of humidified 95% air and 5% CO<sub>2</sub>. The medium was changed every other day, and slices were washed and fixed with 4% PFA for 30 min on day 4 in vitro. For AICAR treatment, the drug was dissolved in water at 1 mM concentration; water was used as vehicle. For Torin1 treatment, the drug was dissolved in DMSO at 5  $\mu\text{m}$  concentration; DMSO was used as vehicle for the Torin1 experiments.

### COSC immunohistochemistry

Using a scalpel, the membrane with the slices still attached were cut and, using a brush, transferred into the wells of a 24-well plate containing 1x PBS. The PBS was then replaced with pre-cooled 100% ethanol and slices were incubated at -20 °C for 15 to 20 min. The slices were washed three times in 1x PBS for 10 min at room temperature and incubated for 30 min with a solution containing 1x PBS + 1% Triton-X 100 (1%PBT) and 20% NDS detergent at room temperature. Next, the slices were incubated overnight with the primary antibodies diluted in blocking solution at 4 °C. The primary antibodies used on cerebellar organotypic slices were rabbit anti-pyruvate dehydrogenase E 1 alpha (PDHE1) (1:200, GeneTex, # GTX104015), rat anti-LAMP1 (1:200, BioLegend, 121602) and mouse anti-CALB (calbindin,1:200, Sigma-Aldrich). The corresponding secondary antibodies were then used after three washes with 1X PBT (1:500, Jackson-ImmunoResearch or Invitrogen). Cerebellar sections were then washed three times with 1X PBT for 10–15 min, incubated with DAPI, and mounted in Aqua-Poly/mount (Polysciences).

### Microscope imaging analysis of COSCs

Quantification of PDHE1<sup>+</sup> mitochondria and LAMP1<sup>+</sup> lysosomes total volume per the total volume of CALB<sup>+</sup> dendrites was performed as previously reported<sup>30,90</sup>. As described above, the Imaris software was used to create the 3D surface renderings for 40X confocal images. Images were cropped 250  $\mu\text{m}$  X 450  $\mu\text{m}$  for the analysis.

To determine changes in dendritic tree morphology, COSCs were imaged using a Zeiss LSM 700 laser scanning confocal microscope. A stack of 5 confocal image slices (each 1  $\mu\text{m}$  in depth) were combined to make 1 3D image per COSC. Each 3D image was cropped to 550  $\mu\text{m}$  X 370  $\mu\text{m}$ , Z=5  $\mu\text{m}$ . Quantitative analysis of the 3D dendritic morphology was performed using the Filaments tracer tool of the Imaris 9.9.1 software and 6–10 confocal images per genotype/treatment.

### Neonatal ambulation motor test

Ambulation of P8 Control and *Pten* cKO mice was analyzed as previously described<sup>35</sup>. Individual mouse pups were placed over an open, clean surface where they were visible from the top as well as the side. Pups were gently touched on the tail to motivate them to move. During the test, the pups were video recorded for 3 min, then investigators blinded to the genotype analyzed the videos and identified ambulation as crawling, transition to walking, and no movement. For this test, the pups were briefly separated from their mother for the 3-minute video recording and were promptly reunited with her afterward.

Transition from crawling to walking was identified by observing the hind paw. Contrary to crawling, where the whole hind paw touches the ground during ambulation, in transition to walking only the front part of the hind paw touches the ground (elevated heel)<sup>35</sup>. The ambulation of the pups was further analyzed and scored using the following scale: 1 = crawling/transition with asymmetric limb movement, and 2 = crawling/transition.

### Juvenile play-social interactions test

Mice were housed in standard conditions and allowed to acclimate to their environment before testing. A P21 Control or Pten cKO mouse was placed in an empty new cage with an unfamiliar wild-type (C57Bl/6j) female mouse of similar age and video recorded for at least 15 min. Social (nose-to-nose, anogenital sniffing, following, crawling under) and non-social (exploring cage, wall rearing, sitting alone, self-grooming) behaviors were scored based on frequency or duration criteria as described previously<sup>39,40</sup>; investigators were blind to the mouse genotype during scoring analysis.

### Ladder rung walking task

The ladder rung walking test was performed as previously reported<sup>30</sup>. The test consisted of mice traversing sections with 1 cm spacing at the start and end of the test but encountering a challenging 22 cm central stretch with 2 cm spacing between rungs where slips and misses were quantified. Each mouse was individually placed at one end of the ladder and filmed from the side as it walked across the ladder from start to finish. The video recordings were analyzed by independent investigators who were unaware of the mice's genotypes. The investigators quantified the number of misses and slips of both forelimbs and hindlimbs specifically in the section with the 2 cm spacing. The task was performed three times for each mouse, and the performance data from the three trials was summed.

### Statistical analysis

Analysis of data was performed using the GraphPad Prism software. Statistical significance was calculated using unpaired t-tests for comparisons between two groups or One-Way ANOVA for multiple comparisons. Fisher's exact test was used to calculate statistical significance between proportions of the categories in two group variables. p-values are provided as stated by GraphPad Prism software and significance was determined with p-values less than 0.05. Holm-Sidak method for correction of multiple comparisons was selected in GraphPad Prism software specifically for the Sholl analysis.

### Data availability

All data generated or analyzed during this study are included in this published article [and its supplementary information files].

Received: 18 March 2025; Accepted: 25 June 2025

Published online: 08 July 2025

### References

1. Ciaccio, C. et al. Clinical spectrum of PTEN mutation in pediatric patients. A bicenter experience. *Eur. J. Med. Genet.* **62**, 103596. <https://doi.org/10.1016/j.ejmg.2018.12.001> (2019).
2. Hansen-Kiss, E. et al. A retrospective chart review of the features of PTEN Hamartoma tumour syndrome in children. *J. Med. Genet.* **54**, 471–478. <https://doi.org/10.1136/jmedgenet-2016-104484> (2017).
3. Frazier, T. W. et al. Molecular and phenotypic abnormalities in individuals with germline heterozygous PTEN mutations and autism. *Mol. Psychiatry.* **20**, 1132–1138. <https://doi.org/10.1038/mp.2014.125> (2015).
4. Tariq, K. et al. Disruption of mTORC1 rescues neuronal overgrowth and synapse function dysregulated by Pten loss. *Cell. Rep.* **41**, 111574. <https://doi.org/10.1016/j.celrep.2022.111574> (2022).
5. Panzenhagen, A. C. et al. Behavioral manifestations in rodent models of autism spectrum disorder: protocol for a systematic review and network meta-analysis. *Syst. Rev.* **11**, 150. <https://doi.org/10.1186/s13643-022-02028-w> (2022).
6. Chai, A. P. et al. A Temporal activity of CA1 neurons underlying Short-Term memory for social recognition altered in PTEN mouse models of autism spectrum disorder. *Front. Cell. Neurosci.* **15**, 699315. <https://doi.org/10.3389/fncel.2021.699315> (2021).
7. Feng, C. et al. PTEN regulates mitochondrial biogenesis via the AKT/GSK-3beta/PGC-1alpha pathway in autism. *Neuroscience* **465**, 85–94. <https://doi.org/10.1016/j.neuroscience.2021.04.010> (2021).
8. Shin, S., Santi, A. & Huang, S. Conditional Pten knockout in parvalbumin- or somatostatin-positive neurons sufficiently leads to autism-related behavioral phenotypes. *Mol. Brain.* **14**, 24. <https://doi.org/10.1186/s13041-021-00731-8> (2021).
9. Binder, M. S. & Lugo, J. N. NS-Pten knockout mice show sex- and age-specific differences in ultrasonic vocalizations. *Brain Behav.* **7**, e00857. <https://doi.org/10.1002/brb3.857> (2017).
10. Huang, W. C., Chen, Y. & Page, D. T. Hyperconnectivity of prefrontal cortex to amygdala projections in a mouse model of macrocephaly/autism syndrome. *Nat. Commun.* **7**, 13421. <https://doi.org/10.1038/ncomms13421> (2016).
11. Kwon, C. H. et al. Pten regulates neuronal arborization and social interaction in mice. *Neuron* **50**, 377–388. <https://doi.org/10.1016/j.neuron.2006.03.023> (2006).
12. Cupolillo, D. et al. Autistic-Like traits and cerebellar dysfunction in Purkinje cell PTEN Knock-Out mice. *Neuropsychopharmacology* **41**, 1457–1466. <https://doi.org/10.1038/npp.2015.339> (2016).
13. Chao, O. Y., Zhang, H., Pathak, S. S., Huston, J. P. & Yang, Y. M. Functional convergence of motor and social processes in lobule IV/V of the mouse cerebellum. *Cerebellum* **20**, 836–852. <https://doi.org/10.1007/s12311-021-01246-7> (2021).
14. Crippa, A. et al. Cortico-Cerebellar connectivity in autism spectrum disorder: what do we know so far?? *Front. Psychiatry* **7**, 20. <https://doi.org/10.3389/fpsyg.2016.00020> (2016).
15. van der Heijden, M. E., Gill, J. S. & Sillitoe, R. V. Abnormal cerebellar development in autism spectrum disorders. *Dev. Neurosci.* **43**, 181–190. <https://doi.org/10.1159/000515189> (2021).
16. Peter, S. et al. Dysfunctional cerebellar Purkinje cells contribute to autism-like behaviour in Shank2-deficient mice. *Nat. Commun.* **7**, 12627. <https://doi.org/10.1038/ncomms12627> (2016).
17. Sudarov, A. Defining the role of cerebellar Purkinje cells in autism spectrum disorders. *Cerebellum* **12**, 950–955. <https://doi.org/10.1007/s12311-013-0490-y> (2013).
18. Tsai, P. T. et al. Autistic-like behaviour and cerebellar dysfunction in Purkinje cell Tsc1 mutant mice. *Nature* **488**, 647–651. <https://doi.org/10.1038/nature11310> (2012).
19. Xu, F. X. et al. Purkinje-cell-specific MeCP2 deficiency leads to motor deficits and autistic-like behavior due to aberrations in PTP1B-TrkB-SK signaling. *Cell. Rep.* **42**, 113559. <https://doi.org/10.1016/j.celrep.2023.113559> (2023).
20. Sakai, Y. et al. Hyperactivation of mTORC1 disrupts cellular homeostasis in cerebellar Purkinje cells. *Sci. Rep.* **9**, 2799. <https://doi.org/10.1038/s41598-019-38730-4> (2019).

21. Salman, M. S. & Tsai, P. The role of the pediatric cerebellum in motor functions, cognition, and behavior: A clinical perspective. *Neuroimaging Clin. N. Am.* **26**, 317–329. <https://doi.org/10.1016/j.nic.2016.03.003> (2016).
22. Fukumitsu, K. et al. Synergistic action of dendritic mitochondria and creatine kinase maintains ATP homeostasis and actin dynamics in growing neuronal dendrites. *J. Neurosci.* **35**, 5707–5723. <https://doi.org/10.1523/JNEUROSCI.4115-14.2015> (2015).
23. Ulvhake, B. & Kellerth, J. O. A quantitative light microscopic study of the dendrites of Cat spinal alpha-motoneurons after intracellular staining with horseradish peroxidase. *J. Comp. Neurol.* **202**, 571–583. <https://doi.org/10.1002/cne.902020409> (1981).
24. Howell, J. J. & Manning, B. D. mTOR couples cellular nutrient sensing to organismal metabolic homeostasis. *Trends Endocrinol. Metab.* **22**, 94–102. <https://doi.org/10.1016/j.tem.2010.12.003> (2011).
25. Urbanska, M., Gozdz, A., Swiech, L. J. & Jaworski, J. Mammalian target of Rapamycin complex 1 (mTORC1) and 2 (mTORC2) control the dendritic arbor morphology of hippocampal neurons. *J. Biol. Chem.* **287**, 30240–30256. <https://doi.org/10.1074/jbc.M112.374405> (2012).
26. Li, S., Zhang, C., Takemori, H., Zhou, Y. & Xiong, Z. Q. TORC1 regulates activity-dependent CREB-target gene transcription and dendritic growth of developing cortical neurons. *J. Neurosci.* **29**, 2334–2343. <https://doi.org/10.1523/JNEUROSCI.2296-08.2009> (2009).
27. Angliker, N., Burri, M., Zaichuk, M., Fritschy, J. M. & Ruegg, M. A. mTORC1 and mTORC2 have largely distinct functions in Purkinje cells. *Eur. J. Neurosci.* **42**, 2595–2612. <https://doi.org/10.1111/ejn.13051> (2015).
28. Carracedo, A. & Pandolfi, P. P. The PTEN-PI3K pathway: of feedbacks and cross-talks. *Oncogene* **27**, 5527–5541. <https://doi.org/10.1038/onc.2008.247> (2008).
29. Papa, A. & Pandolfi, P. P. The PTEN(-)PI3K Axis in Cancer. *Biomolecules* **9** <https://doi.org/10.3390/biom9040153> (2019).
30. Kim, S. et al. Disruptive lysosomal-metabolic signaling and neurodevelopmental deficits that precede Purkinje cell loss in a mouse model of Niemann-Pick Type-C disease. *Sci. Rep.* **13**, 5665. <https://doi.org/10.1038/s41598-023-32971-0> (2023).
31. Markant, J. C. & Thomas, K. M. *Postnatal Brain Development*. Oxford Academic (2013).
32. Lachyankar, M. B. et al. A role for nuclear PTEN in neuronal differentiation. *J. Neurosci.* **20**, 1404–1413. <https://doi.org/10.1523/JNEUROSCI.20-04-01404.2000> (2000).
33. Perandones, C. et al. Correlation between synaptogenesis and the PTEN phosphatase expression in dendrites during postnatal brain development. *Brain Res. Mol. Brain Res.* **128**, 8–19. <https://doi.org/10.1016/j.molbrainres.2004.05.021> (2004).
34. Jahncke, J. N. & Wright, K. M. Tools for Cre-Mediated Conditional Deletion of Floxed Alleles from Developing Cerebellar Purkinje Cells. *eNeuro* **11**. <https://doi.org/10.1523/ENEURO.0149-24.2024> (2024).
35. Feather-Schussler, D. N. & Ferguson, T. S. A battery of motor tests in a neonatal mouse model of cerebral palsy. *J. Vis. Exp.* <https://doi.org/10.3791/53569> (2016).
36. Carter, A. S. et al. Sex differences in toddlers with autism spectrum disorders. *J. Autism Dev. Disord.* **37**, 86–97. <https://doi.org/10.1007/s10803-006-0331-7> (2007).
37. Craig, F. et al. Differences in developmental functioning profiles between male and female preschoolers children with autism spectrum disorder. *Autism Res.* **13**, 1537–1547. <https://doi.org/10.1002/aur.2305> (2020).
38. Limperopoulos, C. et al. Does cerebellar injury in premature infants contribute to the high prevalence of long-term cognitive, learning, and behavioral disability in survivors? *Pediatrics* **120**, 584–593. <https://doi.org/10.1542/peds.2007-1041> (2007).
39. Campolongo, M. et al. Sociability deficits after prenatal exposure to valproic acid are rescued by early social enrichment. *Mol. Autism* **9**, 36. <https://doi.org/10.1186/s13229-018-0221-9> (2018).
40. Cox, K. H. & Rissman, E. F. Sex differences in juvenile mouse social behavior are influenced by sex chromosomes and social context. *Genes Brain Behav.* **10**, 465–472. <https://doi.org/10.1111/j.1601-183X.2011.00688.x> (2011).
41. Hollander, M. C., Blumenthal, G. M. & Dennis, P. A. PTEN loss in the continuum of common cancers, rare syndromes and mouse models. *Nat. Rev. Cancer.* **11**, 289–301. <https://doi.org/10.1038/nrc3037> (2011).
42. Biever, A., Valjent, E., Puighermanal, E. & Ribosomal Protein, S. 6 phosphorylation in the nervous system: from regulation to function. *Front. Mol. Neurosci.* **8**, 75. <https://doi.org/10.3389/fnmol.2015.00075> (2015).
43. Carayol, N. et al. Critical roles for mTORC2- and rapamycin-insensitive mTORC1-complexes in growth and survival of BCR-ABL-expressing leukemic cells. *Proc. Natl. Acad. Sci. U. S. A.* **107**, 12469–12474. <https://doi.org/10.1073/pnas.1005114107> (2010).
44. Figueiredo, V. C., Markworth, J. F. & Cameron-Smith, D. Considerations on mTOR regulation at Serine 2448: implications for muscle metabolism studies. *Cell. Mol. Life Sci.* **74**, 2537–2545. <https://doi.org/10.1007/s00018-017-2481-5> (2017).
45. Davis, O. B. et al. NPC1-mTORC1 signaling couples cholesterol sensing to organelle homeostasis and is a targetable pathway in Niemann-Pick type C. *Dev. Cell.* **56**, 260–276. <https://doi.org/10.1016/j.devcel.2020.11.016> (2021).
46. Puertollano, R. mTOR and lysosome regulation. *F1000Prime Rep.* **6**, 52. <https://doi.org/10.12703/P6-52> (2014).
47. Herzig, S. & Shaw, R. J. AMPK: guardian of metabolism and mitochondrial homeostasis. *Nat. Rev. Mol. Cell. Biol.* **19**, 121–135. <https://doi.org/10.1038/nrm.2017.95> (2018).
48. Kahn, B. B., Alquier, T., Carling, D. & Hardie, D. G. AMP-activated protein kinase: ancient energy gauge provides clues to modern Understanding of metabolism. *Cell. Metab.* **1**, 15–25. <https://doi.org/10.1016/j.cmet.2004.12.003> (2005).
49. Shaw, R. J. LKB1 and AMP-activated protein kinase control of mTOR signalling and growth. *Acta Physiol.* **196**, 65–80. <https://doi.org/10.1111/j.1748-1716.2009.01972.x> (2009).
50. Smiles, W. J. et al. New developments in AMPK and mTORC1 cross-talk. *Essays Biochem.* <https://doi.org/10.1042/EBC20240007> (2024).
51. Kim, J., Yang, G., Kim, Y., Kim, J. & Ha, J. AMPK activators: mechanisms of action and physiological activities. *Exp. Mol. Med.* **48**, e224. <https://doi.org/10.1038/emm.2016.16> (2016).
52. Yu, L. & Yang, S. J. AMP-activated protein kinase mediates activity-dependent regulation of peroxisome proliferator-activated receptor gamma coactivator-1alpha and nuclear respiratory factor 1 expression in rat visual cortical neurons. *Neuroscience* **169**, 23–38. <https://doi.org/10.1016/j.neuroscience.2010.04.063> (2010).
53. Paquette, M. et al. AMPK-dependent phosphorylation is required for transcriptional activation of TFEB and TFE3. *Autophagy* **17**, 3957–3975. <https://doi.org/10.1080/15548627.2021.1898748> (2021).
54. Morita, M. et al. mTOR Controls Mitochondrial Dynamics and Cell Survival via MTFP1. *Mol. Cell.* **67**, 922–935. <https://doi.org/10.1016/j.molcel.2017.08.013> (2017).
55. Frazier, T. W. Autism spectrum disorder associated with germline heterozygous PTEN mutations. *Cold Spring Harb. Perspect. Med.* **9** <https://doi.org/10.1101/cshperspect.a037002> (2019).
56. Hazlett, H. C. et al. Early brain development in infants at high risk for autism spectrum disorder. *Nature* **542**, 348–351. <https://doi.org/10.1038/nature21369> (2017).
57. Lainhart, J. E. et al. Head circumference and height in autism: a study by the collaborative program of excellence in autism. *Am. J. Med. Genet. A.* **140**, 2257–2274. <https://doi.org/10.1002/ajmg.a.31465> (2006).
58. Dusart, I. & Flamant, F. Profound morphological and functional changes of rodent Purkinje cells between the first and the second postnatal weeks: a metamorphosis? *Front. Neuroanat.* **6**, 11. <https://doi.org/10.3389/fnana.2012.00011> (2012).
59. Sotelo, C. & Dusart, I. Intrinsic versus extrinsic determinants during the development of Purkinje cell dendrites. *Neuroscience* **162**, 589–600. <https://doi.org/10.1016/j.neuroscience.2008.12.035> (2009).
60. Gonzalez, A., Moya-Alvaredo, G., Gonzalez-Billaut, C. & Bronfman, F. C. Cellular and molecular mechanisms regulating neuronal growth by brain-derived neurotrophic factor. *Cytoskeleton (Hoboken)* **73**, 612–628. <https://doi.org/10.1002/cm.21312> (2016).
61. Carter, A. R., Chen, C., Schwartz, P. M. & Segal, R. A. Brain-derived neurotrophic factor modulates cerebellar plasticity and synaptic ultrastructure. *J. Neurosci.* **22**, 1316–1327. <https://doi.org/10.1523/JNEUROSCI.22-04-01316.2002> (2002).

62. Neveu, I. & Arenas, E. Neurotrophins promote the survival and development of neurons in the cerebellum of hypothyroid rats in vivo. *J. Cell. Biol.* **133**, 631–646. <https://doi.org/10.1083/jcb.133.3.631> (1996).
63. Bao, S., Chen, L., Qiao, X. & Thompson, R. F. Transgenic brain-derived neurotrophic factor modulates a developing cerebellar inhibitory synapse. *Learn. Mem.* **6**, 276–283 (1999).
64. Moya-Alvarez, G. et al. BDNF/TrkB signaling endosomes in axons coordinate creb/mtr activation and protein synthesis in the cell body to induce dendritic growth in cortical neurons. *Elife* **12** <https://doi.org/10.7554/elife.77455> (2023).
65. Nayeem, N. et al. Hyperphosphorylation of Tau and neurofilaments and activation of CDK5 and ERK1/2 in PTEN-deficient cerebella. *Mol. Cell. Neurosci.* **34**, 400–408. <https://doi.org/10.1016/j.mcn.2006.11.014> (2007).
66. Didonna, A. & Opal, P. The role of neurofilament aggregation in neurodegeneration: lessons from rare inherited neurological disorders. *Mol. Neurodegener.* **14**, 19. <https://doi.org/10.1186/s13024-019-0318-4> (2019).
67. Fournier, K. A., Hass, C. J., Naik, S. K., Lodha, N. & Cauraugh, J. H. Motor coordination in autism spectrum disorders: a synthesis and meta-analysis. *J. Autism Dev. Disord.* **40**, 1227–1240. <https://doi.org/10.1007/s10803-010-0981-3> (2010).
68. Phillips, J. R., Hewedi, D. H., Eissa, A. M. & Moustafa, A. A. The cerebellum and psychiatric disorders. *Front. Public Health.* **3**, 66. <https://doi.org/10.3389/fpubh.2015.00066> (2015).
69. Teitelbaum, P., Teitelbaum, O., Nye, J., Fryman, J. & Maurer, R. G. Movement analysis in infancy May be useful for early diagnosis of autism. *Proc. Natl. Acad. Sci. U. S. A.* **95**, 13982–13987. <https://doi.org/10.1073/pnas.95.23.13982> (1998).
70. Busch, R. M. et al. Neurobehavioral phenotype of autism spectrum disorder associated with germline heterozygous mutations in PTEN. *Transl. Psychiatry* **9**, 253. <https://doi.org/10.1038/s41398-019-0588-1> (2019).
71. Cummings, K., Watkins, A., Jones, C., Dias, R. & Welham, A. Behavioural and psychological features of PTEN mutations: a systematic review of the literature and meta-analysis of the prevalence of autism spectrum disorder characteristics. *J. Neurodev. Disord.* **14**, 1. <https://doi.org/10.1186/s11689-021-09406-w> (2022).
72. Zwaigenbaum, L., Bryson, S. & Garon, N. Early identification of autism spectrum disorders. *Behav. Brain Res.* **251**, 133–146. <https://doi.org/10.1016/j.bbr.2013.04.004> (2013).
73. Elsabbagh, M. et al. Infant neural sensitivity to dynamic eye gaze is associated with later emerging autism. *Curr. Biol.* **22**, 338–342. <https://doi.org/10.1016/j.cub.2011.12.056> (2012).
74. Garon, N., Bryson, S. E. & Zwaigenbaum, L. In *Handbook of Autism Spectrum Disorder and Pervasive Developmental Disorders* JL Matson (eds) 239–258 (2009).
75. West, K. L., Leezenbaum, N. B., Northrup, J. B. & Iverson, J. M. The relation between walking and Language in infant siblings of children with autism spectrum disorder. *Child. Dev.* **90**, e356–e372. <https://doi.org/10.1111/cdev.12980> (2019).
76. Bhat, A. Multidimensional motor performance in children with autism mostly remains stable with age and predicts social communication delay, Language delay, functional delay, and repetitive behavior severity after accounting for intellectual disability or cognitive delay: A SPARK dataset analysis. *Autism Res.* **16**, 208–229. <https://doi.org/10.1002/aur.2870> (2023).
77. Manto, M. & Marien, P. Schmahmann's syndrome - identification of the third cornerstone of clinical ataxiology. *Cereb. Ataxias.* **2**, 2. <https://doi.org/10.1186/s40673-015-0023-1> (2015).
78. Thach, W. T. What is the role of the cerebellum in motor learning and cognition? *Trends Cogn. Sci.* **2**, 331–337. [https://doi.org/10.1016/s1364-6613\(98\)01223-6](https://doi.org/10.1016/s1364-6613(98)01223-6) (1998).
79. Ivankovic, D., Chau, K. Y., Schapira, A. H. & Gegg, M. E. Mitochondrial and lysosomal biogenesis are activated following PINK1/parkin-mediated mitophagy. *J. Neurochem.* **136**, 388–402. <https://doi.org/10.1111/jnc.13412> (2016).
80. Zhu, J., Wang, K. Z. & Chu, C. T. After the banquet: mitochondrial biogenesis, mitophagy, and cell survival. *Autophagy* **9**, 1663–1676. <https://doi.org/10.4161/auto.24135> (2013).
81. Bordi, M. et al. mTOR hyperactivation in down syndrome underlies deficits in autophagy induction, autophagosome formation, and mitophagy. *Cell Death Dis.* **10**, 563. <https://doi.org/10.1038/s41419-019-1752-5> (2019).
82. Ling, N. X. Y. et al. mTORC1 directly inhibits AMPK to promote cell proliferation under nutrient stress. *Nat. Metab.* **2**, 41–49. <https://doi.org/10.1038/s42255-019-0157-1> (2020).
83. Kovacic, S. et al. Akt activity negatively regulates phosphorylation of AMP-activated protein kinase in the heart. *J. Biol. Chem.* **278**, 39422–39427. <https://doi.org/10.1074/jbc.M305371200> (2003).
84. Palmieri, M. et al. mTORC1-independent TFEB activation via Akt Inhibition promotes cellular clearance in neurodegenerative storage diseases. *Nat. Commun.* **8**, 14338. <https://doi.org/10.1038/ncomms14338> (2017).
85. Srivastava, S. et al. A randomized controlled trial of everolimus for neurocognitive symptoms in PTEN Hamartoma tumor syndrome. *Hum. Mol. Genet.* **31**, 3393–3404. <https://doi.org/10.1093/hmg/ddac111> (2022).
86. Gantois, I., Popic, J., Khoutorsky, A. & Sonenberg, N. Metformin for treatment of fragile X syndrome and other neurological disorders. *Annu. Rev. Med.* **70**, 167–181. <https://doi.org/10.1146/annurev-med-081117-041238> (2019).
87. Urbinati, C. et al. Chronic treatment with the anti-diabetic drug Metformin rescues impaired brain mitochondrial activity and selectively ameliorates defective cognitive flexibility in a female mouse model of Rett syndrome. *Neuropharmacology* **224**, 109350. <https://doi.org/10.1016/j.neuropharm.2022.109350> (2023).
88. Beekhof, G. C. et al. Differential Spatiotemporal development of Purkinje cell populations and cerebellum-dependent sensorimotor behaviors. *Elife* **10** <https://doi.org/10.7554/elife.63668> (2021).
89. Zhong, F., Liu, L., Wei, J. L. & Dai, R. P. Step by step Golgi-Cox staining for Cryosection. *Front. Neuroanat.* **13**, 62. <https://doi.org/10.3389/fnana.2019.00062> (2019).
90. MacLeod, C. M. et al. Trehalose enhances mitochondria deficits in human NPC1 mutant fibroblasts but disrupts mouse Purkinje cell dendritic growth ex vivo. *PLoS One.* **18**, e0294312. <https://doi.org/10.1371/journal.pone.0294312> (2023).

## Acknowledgements

NSF-Division of Integrative Organismal Systems, NSF-IOS1941296.

## Author contributions

L.J.W, I.M.E, A.V.R, U.M.P, K.E.F, W.C.R, S.R.B, N.I.A, A. J.C., and T.A.D performed experiments and analyzed data. I.S. designed all the experiments, oversaw data generation and analysis, and wrote the manuscript. All authors reviewed and approved the final version.

## Declarations

### Competing interests

The authors declare no competing interests.

### Additional information

**Supplementary Information** The online version contains supplementary material available at <https://doi.org/10.1038/s41598-025-09059-y>.

**Correspondence** and requests for materials should be addressed to I.S.

**Reprints and permissions information** is available at [www.nature.com/reprints](http://www.nature.com/reprints).

**Publisher's note** Springer Nature remains neutral with regard to jurisdictional claims in published maps and institutional affiliations.

**Open Access** This article is licensed under a Creative Commons Attribution-NonCommercial-NoDerivatives 4.0 International License, which permits any non-commercial use, sharing, distribution and reproduction in any medium or format, as long as you give appropriate credit to the original author(s) and the source, provide a link to the Creative Commons licence, and indicate if you modified the licensed material. You do not have permission under this licence to share adapted material derived from this article or parts of it. The images or other third party material in this article are included in the article's Creative Commons licence, unless indicated otherwise in a credit line to the material. If material is not included in the article's Creative Commons licence and your intended use is not permitted by statutory regulation or exceeds the permitted use, you will need to obtain permission directly from the copyright holder. To view a copy of this licence, visit <http://creativecommons.org/licenses/by-nc-nd/4.0/>.

© The Author(s) 2025